# Structural Basis for Selectivity and Diversity in Angiotensin II Receptors

**Haitao Zhang**[1,2], **Gye Won Han**[1], **Alexander Batyuk**[3], **Andrii Ishchenko**[1], **Kate L. White**[1,4], **Nilkanth Patel**[4], **Anastasiia Sadybekov**[1], **Beata Zamlynny**[5], **Michael T. Rudd**[6], **Kaspar Hollenstein**[6], **Alexandra Tolstikova**[7], **Thomas A. White**[7], **Mark S. Hunter**[3], **Uwe Weierstall**[8], **Wei Liu**[9], **Kerim Babaoglu**[6], **Eric L. Moore**[6], **Ryan D. Katz**[10], **Jennifer M. Shipman**[10], **Margarita Garcia-Calvo**[5], **Sujata Sharma**[10], **Payal Sheth**[5], **Stephen M. Soisson**[6], **Raymond C. Stevens**[1,4], **Vsevolod Katritch**[4,*], and **Vadim Cherezov**[1,*]

[1]Department of Chemistry, Bridge Institute, University of Southern California, Los Angeles, California 90089, USA

[2]Institute of Pharmacology and Toxicology, College of Pharmaceutical Sciences, Zhejiang University, 866 Yuhangtang Road, Hangzhou, Zhejiang 310058, China

[3]Linac Coherent Light Source, SLAC National Accelerator Laboratory, 2575 Sand Hill Road, Menlo Park, CA 94025, USA

[4]Department of Biological Sciences, Bridge Institute, University of Southern California, Los Angeles, CA 90089, USA

[5]MRL, Merck & Co., Inc., 2015 Galloping Hill Road, Kenilworth, NJ 07033, USA

[6]MRL, Merck & Co., Inc., 770 Sumneytown Pike, West Point, PA 19486, USA

[7]Center for Free Electron Laser Science, Deutsches Elektronen-Synchrotron DESY, 22607 Hamburg, Germany

[8]Department of Physics, Arizona State University, Tempe, AZ 85287, USA

[9]Department of Chemistry and Biochemistry, and Center for Applied Structural Discovery at the Biodesign Institute, Arizona State University, Tempe, AZ 85287, USA

[10]MRL, Merck & Co., Inc., 503 Louise Lane, North Wales, PA 19454, USA

## Abstract

Angiotensin II receptors, $AT_1R$ and $AT_2R$, serve as key components of the renin-angiotensin-aldosterone system. While $AT_1R$ plays a central role in the regulation of blood pressure, the function of $AT_2R$ is enigmatic with a variety of reported effects. To elucidate the mechanisms for the functional diversity and ligand selectivity between these receptors, we report crystal structures of the human $AT_2R$ bound to an $AT_2R$-selective and an $AT_1R/AT_2R$-dual ligand, respectively, capturing the receptor in an active-like conformation. Unexpectedly, helix VIII was found in a non-canonical position, stabilizing the active-like state, but at the same time preventing the recruitment of G proteins/β-arrestins, in agreement with the lack of signaling responses in standard cellular assays. Structure-activity relationship, docking and mutagenesis studies revealed the interactions critical for ligand binding and selectivity. Our results thus provide insights into the structural basis for distinct functions of the angiotensin receptors, and may guide the design of novel selective ligands.

In humans, the effects of the octapeptide hormone angiotensin II (AngII) are mediated by two types of AngII receptors, $AT_1R$ and $AT_2R$, which share approximately 34% amino acid sequence identity[1,2]. $AT_1R$ is mainly responsible for blood pressure regulation, with several antagonists and inverse agonists approved for clinical use as anti-hypertensive drugs[3]. The function of $AT_2R$, on the other hand, is less understood and remains controversial, with a growing number of studies suggesting that $AT_2R$ signals primarily via non-canonical, G protein- and β-arrestin-independent pathways[4,5]. In the cardiovascular system, $AT_2R$ has been reported to counteract several of the effects mediated by $AT_1R$[6,7], conferring cardioprotection. For example, in vasculature $AT_2R$ has been suggested to counter-balance blood pressure elevation exerted by $AT_1R$[8,9]. It has also been reported that activation of $AT_2R$ in cardiomyocytes inhibits autophagy mediated by $AT_1R$[10]. Moreover, in the central nervous system, $AT_2R$ has been implicated in $AT_1R$-independent signaling pathways[11–14]. It has been observed that activation of $AT_2R$ in nociceptive neurons induces neurite outgrowth and elongation[15], while studies in sensory neurons selectively expressing $AT_2R$ but not $AT_1R$, also supported involvement of $AT_2R$ in nociception[16–18]. Further interest in $AT_2R$ as a drug target has been sparkled by the recent finding that the canonical $AT_2R$ antagonist PD123319 blocks AngII-induced neuronal excitability, and exhibits oral bioavailability in several neuropathic pain models in rodents[17–19]. Most excitingly, EMA401, an analog of PD123319, demonstrated efficacy in phase II clinical trials in patients with post-herpetic neuralgia[16,20]. Interestingly, activation of $AT_2R$ by its small molecule agonist Compound 21 (ref. 21) has also been reported to produce a number of beneficial *in vivo* effects such as inducing pressure natriuresis, lowering blood pressure, conferring acute vaso-relaxation, and exhibiting organ protective effects[22,23].

We previously reported crystal structures of $AT_1R$ in complex with an antagonist ZD7155 (ref. 24) and with an inverse agonist olmesartan[25], which provided insights into $AT_1R$ receptor-ligand interactions. The molecular mechanisms of functional diversity and ligand selectivity between $AT_1R$ and $AT_2R$, however, remain elusive. With an increasing body of evidence indicating that selective targeting of $AT_2R$ could be used for cardioprotection and

for the treatment of neuropathic pain, there is an imminent need to elucidate the structural basis for the functional role of this receptor, and to develop type-selective ligands. In this study, we determined crystal structures of $AT_2R$ bound to two high-affinity ligands, an $AT_2R$-selective ligand compound **1** (Cpd **1**)[26] and an $AT_1R/AT_2R$-dual ligand compound **2** (Cpd **2**)[27]. Both compounds are derivatives of a series of small-molecule antagonists of $AT_1R$ and thus could be assumed to exert the same function in $AT_2R$. However, classification of compounds using traditional G protein-coupled receptor (GPCR) nomenclature into antagonists or agonists has proven difficult for $AT_2R$ since it has not been reliably demonstrated to signal through any of the canonical GPCR signaling pathways involving G proteins or β-arrestin. Furthermore, it has been observed numerous times that small changes to the structures of closely related compounds can lead to changes or bias in function[28,29]. Therefore, we refer to Cpd **1** and Cpd **2** using the neutral term 'ligand'. In addition to a dramatic reshaping of the ligand-binding pocket between the two receptors, our $AT_2R$ structures revealed an active-like conformation of the seven-transmembrane (7TM) helical bundle with a non-canonical positioning of the amphipathic helix VIII, potentially blocking recruitment of intracellular signaling partners.

## Structure determination

The human $AT_2R$ construct used for structure determination was engineered to facilitate crystallization (Extended Data Fig. 1) by truncating the N-terminal residues 1–34 and the C-terminal residues 336–363, and fusing a thermostabilized apocytochrome $b_{562}RIL$[30] to the truncated N-terminus via a 4-residue linker. Compared to wild-type $AT_2R$, the engineered receptor showed no significant difference in the binding to small molecule ligands (Cpds **1** and **2**) as determined by radio-ligand binding assays (Extended Data Fig. 2a,c,d). In contrast, the affinities of the peptides AngII and Sar$^1$-Ile$^8$-AngII were slightly lower (~3-fold), a potential consequence of the N-terminal truncation (Extended Data Fig. 2b). $AT_2R$ bound to the selective ligand Cpd **1** generated a high density of microcrystals in lipidic cubic phase (LCP)[31] with an average size of 5×2×2 μm$^3$ (Extended Data Fig. 3a). These microcrystals were used to collect serial femtosecond crystallography (SFX)[32–34] data at an X-ray free-electron laser (XFEL), resulting in two 2.8 Å resolution room temperature structures solved in monoclinic and orthorhombic space groups, respectively (Extended Data Table 1). In parallel, we solved another $AT_2R$ structure in complex with the non-selective $AT_1R/AT_2R$ dual ligand Cpd **2** at 2.9 Å resolution (Extended Data Table 1) by synchrotron radiation, using cryo-cooled crystals with an average size of 70×40×20 μm$^3$ (Extended Data Fig. 3b). All three $AT_2R$ structures showed nearly identical conformations of the receptor (RMSD$_{C\alpha}$ < 0.5 Å). Since the orthorhombic $AT_2R$-Cpd **1** structure is the most complete, we used it for the description of the overall $AT_2R$ structure below, unless noted otherwise.

## Active-like conformation of 7TM bundle

The overall architecture of $AT_2R$ is comprised of a 7TM bundle (helices I–VII) and an intracellular amphipathic helix VIII (Fig. 1a). Similar to $AT_1R$ and other peptide-binding GPCRs[24], $AT_2R$ exhibits a β-hairpin conformation of the extracellular loop 2 (ECL2) and two pairs of disulfide bonds linking the N-terminus with ECL3 (Cys35$^{N-term}$-Cys290$^{ECL3}$), and helix III with ECL2 (Cys117$^{3.25}$-Cys195$^{ECL2}$, superscripts indicate residue numbers as

per the Ballesteros-Weinstein nomenclature[35]). A closer comparison of the $AT_1R$ and $AT_2R$ structures, however, revealed substantially different conformations (Fig. 1b–e). While the previously determined $AT_1R$ structures captured the receptor in a classical inactive state, all three $AT_2R$ structures, obtained in this work, display an active-like conformation. Specifically, the intracellular end of helix VI shows an outward displacement by ~11.5 Å, whereas the intracellular end of helix VII exhibits an inward displacement by ~4.9 Å, as compared to the structures of inactive $AT_1R$ (Fig. 1e). Similar large-scale shifts of helices VI and VII that open an intracellular cleft for the recruitment of G proteins/β-arrestins have been implicated in activation of all class A GPCRs[36,37]. Another major conformational rearrangement occurs at the extracellular end of helix V, which is shifted toward the ligand-binding pocket by ~4.8 Å, compared to $AT_1R$ (Fig. 1d). Similar shifts of the extracellular part of helix V, although typically with a smaller ~2 Å amplitude, have been observed in structures of several activated GPCRs, such as the $β_2$-adrenergic ($β_2AR$) and serotonin 5-$HT_{2B}$ receptors[38,39]. Such agonist-stabilized displacement of helix V is critical for triggering re-arrangements in the $P^{5.50}$-$I^{3.40}$-$F^{6.44}$ motif leading to activation of these receptors[38–40].

The large-scale re-arrangements of helices during activation are accompanied by conformational changes in the conserved micro-switches[36]. We therefore compared the $DR^{3.50}Y$, $NP^{7.50}xxY$, and $P^{5.50}$-$I^{3.40}$-$F^{6.44}$ motifs of $AT_2R$ with those in the structures of inactive $AT_1R$ and of fully activated GPCRs, such as $G_s$ protein-bound $β_2AR$[38] and arrestin-bound rhodopsin[38,41]. The large-scale movement of helix VI upon activation is enabled by re-arrangements in the $P^{5.50}$-$I^{3.40}$-$F^{6.44}$ motif ($Pro223^{5.50}$-$Ile132^{3.40}$-$Phe265^{6.44}$ in $AT_2R$) as it was previously demonstrated in other structures of activated GPCRs (Fig. 1c). In the $DR^{3.50}Y$ motif, the $Arg142^{3.50}$ side chain of $AT_2R$ is rotated by ~90° compared to $Arg126^{3.50}$ in $AT_1R$, adopting a similar conformation as in other fully activated GPCRs. Additionally, in the $NP^{7.50}xxY$ motif, the side chain of $Tyr318^{7.53}$ is shifted by ~6.5 Å and rotated by ~45° from the corresponding position of $Tyr302^{7.53}$ in $AT_1R$, following the inward movement of helix VII, as observed in other receptors upon activation. Finally, analysis of the conserved residue switch[37] in the G protein-binding pocket $L[M]^{3.46}$–$I[A]^{6.37}$–$Y[Y]^{7.53}$ ($AT_2R$ residues are shown in brackets) confirms the rearrangement of interactions in this residue triad consistent with an active-like state of $AT_2R$ (Extended Data Fig. 4a,b). Interestingly, instead of a highly conserved large hydrophobic residue in position 6.37, $AT_2R$ has a rare alanine residue (~3% of class A GPCRs), which drastically reduces the hydrophobic contact area between helices III and VI in the inactive state, and likely facilitates the activation related changes in $AT_2R$. Therefore, all of the major conformational features indicate that the 7TM bundle of $AT_2R$ adopts an active-like conformation, similar to that observed in the crystal structures of other fully activated class A GPCRs bound to signaling partners or their mimics.

In addition to the conserved micro-switches, a sodium-binding site consisting of sixteen highly conserved residues is expected to undergo large-scale conformational changes upon activation of class A GPCRs[42]. Superposition of $AT_2R$ with $AT_1R$ revealed that the putative sodium-binding pocket in $AT_2R$ is collapsed and rearranged, hindering sodium ion binding (Extended Data Fig. 4c,d), primarily due to the inward shift of helix VII, which is consistent with the structures of other activated GPCRs[42]. Only two out of sixteen residues in the putative sodium pocket ($Ile135^{3.43}$ and $Ser311^{7.46}$) are different from their counterparts in

AT$_1$R (Leu119$^{3.43}$ and Asn295$^{7.46}$). Interestingly, Asn295$^{7.46}$Ala mutation was implicated in the AT$_1$R constitutive activation[43,44], potentially due to the disruption of two hydrogen bonds between Asn295$^{7.46}$ and Asn111$^{3.35}$ that stabilize the inactive conformation. In contrast, Ser311$^{7.46}$ in AT$_2$R cannot engage in a similar interaction with Asn127$^{3.35}$, potentially shifting the conformational equilibrium toward the active state. Indeed, AT$_2$R has been reported to have high constitutive activity, and to induce apoptosis even in the absence of AngII stimulation[45,46].

## Helix VIII blocks putative G protein/β-arrestin binding site

In most GPCR structures, helix VIII lies parallel to the membrane pointing outside of the 7TM bundle[24], regardless of the receptor's activation state (Fig. 2a,b). Surprisingly, in the AT$_2$R structures helix VIII adopts a very different conformation by flipping over to interact with the intracellular ends of helices III, V, and VI (Fig. 2c). This non-canonical conformation of helix VIII was found in all AT$_2$R structures determined in this study, regardless of the ligand identity and different crystal packing environments (Extended Data Fig. 3c–e), suggesting it to be likely a genuine feature of AT$_2$R, rather than an artifact of crystallization. Helix VIII forms a highly complementary interface with the intracellular cavity of the 7TM bundle, stabilized by extensive hydrophobic interactions mediated by Phe325$^{8.50}$, Leu329$^{8.54}$, Val332$^{8.57}$, and Phe333$^{8.58}$, as well as by polar interactions between Arg324$^{8.49}$, Gln326$^{8.51}$, and Lys328$^{8.53}$, and helices III, V, and VI (Fig. 2d). Docking and molecular dynamics (MD) simulations suggest that helix VIII stabilizes the active-like conformation of the 7TM bundle of AT$_2$R, while sterically blocking the binding of G proteins and β-arrestins (Fig. 2c), which is consistent with the lack of robust downstream signaling by AT$_2$R as assessed by traditional G protein and β-arrestin assays[4,5]. In MD simulations, helix VIII not only remained in the range of positions within RMSD < 4 Å to the crystallographic structure for a total of 4 μs of unbiased simulation (Extended Data Fig. 5a–c), but also quickly (< 200 ns) and reproducibly (n=4) returned to this conformation after consequent perturbations of its position (Extended Data Fig. 5d,e). Alternatively, when helix VIII was relocated to the position observed in the AT$_1$R structures, it relaxed into a canonical membrane-bound conformation, and this motion was accompanied by an inward shift of the intracellular tip of helix VI towards its position in the inactive state AT$_1$R structure in three out six independent MD runs (Extended Data Fig. 5f–h).

## Insights into AT$_1$R/AT$_2$R ligand selectivity

Many AT$_1$R and AT$_2$R ligands share a biphenyl-tetrazole scaffold important for ligand binding affinity. However, molecular mechanisms for ligand selectivity between the two types of angiotensin receptors remain elusive. Our radioligand competition binding studies with Cpd **2** obtained $K_i$ values of 3.7 nM and 0.35 nM for binding to AT$_1$R and AT$_2$R, respectively, indicating this compound is a dual ligand with only about 10-fold selectivity for AT$_2$R over AT$_1$R. In contrast, Cpd **1** exhibited an approximately 530-fold selectivity towards AT$_2$R, with $K_i$ values of 180 nM and 0.34 nM for AT$_1$R and AT$_2$R, respectively (Extended Data Fig. 2c,e).

In all three $AT_2R$ structures, strong electron density was observed in the orthosteric ligand-binding pocket enabling accurate placement of both Cpds **1** and **2** (Extended Data Fig. 6). We compared the positions and interactions of these compounds bound to $AT_2R$ with two ligands bound to $AT_1R$ (the $AT_1R$ selective antagonist ZD7155, and the $AT_1R$ selective inverse agonist olmesartan) (Fig. 3). Surprisingly, despite the common scaffold the ligands bind to the two receptor types very differently, with only the tetrazole moieties partially overlapping and forming critical hydrogen bonds with an arginine in ECL2 ($Arg167^{ECL2}$ in $AT_1R$ and $Arg182^{ECL2}$ in $AT_2R$). The overall biphenyl-tetrazole scaffold of the $AT_2R$-bound ligands, however, is rotated about 45° as compared to its orientation in the $AT_1R$-bound ligands, forming a distinct interaction pattern (Fig. 3a). Interestingly, $Arg^{ECL2}$, $Tyr^{1.39}$, and $Trp^{2.60}$, previously identified as key residues for ligand binding in $AT_1R$, also provide critical protein-ligand contacts in $AT_2R$, although with different side chain conformers. The side chain of $Trp100^{2.60}$ in $AT_2R$ is shifted ~3.1 Å compared to $Trp84^{2.60}$ in $AT_1R$ to form hydrophobic interactions with the thiophene ring of Cpd **1** and the benzene ring of Cpd **2**, both on the carbonyl side of the $AT_2R$ ligands. On the other side of the carbonyl moiety, $Thr88^{2.64}$ in $AT_1R$ is replaced with $Tyr104^{2.64}$ in $AT_2R$ that forms new hydrophobic interactions with the benzene ring of Cpd **1** and the furan ring of Cpd **2**. Moreover, the tetrazole moiety of the $AT_2R$ ligands is engaged in new polar interactions with $Lys215^{5.42}$, $Thr125^{3.33}$ and $Thr178^{4.60}$ side chains, in addition to $Arg182^{ECL2}$. The bottom part of the ligand-binding pocket in $AT_2R$ is expanded due to a smaller side chain of $Leu93^{2.53}$ compared to $Phe77^{2.53}$ in $AT_1R$ and a ~5.2 Å shift of $Phe308^{7.43}$ compared to $Tyr292^{7.43}$ in $AT_1R$ (Fig. 3b, c). In $AT_1R$, $Tyr292^{7.43}$ forms a hydrogen bond with the backbone of helix III, while in $AT_2R$, $Phe308^{7.43}$ is unable to form this interaction and is shifted over in concert with a pronounced shift in the backbone of helix VII. This rearrangement opens a sub-pocket for the binding of the ethyl and propyl moieties of Cpds **1** and **2**. Overall, these changes result in different shapes of the ligand-binding pocket between the two angiotensin receptors and a deeper ligand binding in $AT_2R$.

To gain additional insights into receptor type selectivity, we modeled an active-like state for $AT_1R$ and an inactive state for $AT_2R$, and performed unrestrained cross-docking of ZD7155, olmesartan, Cpds **1** and **2** into the crystal structures and models of both receptors (Extended Data Fig. 7). The results suggest that while the conformational state of $AT_2R$ has little effect on the ligand binding, the predicted active-like conformation of $AT_1R$ is not compatible with binding of any of the tested ligands, corroborating the status of these ligands as antagonists for $AT_1R$. Furthermore, the binding modes of these ligands are imposed by the distinct shapes of the binding pockets of the two receptors. Indeed, the biphenyl-tetrazole moieties of Cpds **1** and **2** docked to $AT_1R$ crystal structure strongly preferred binding modes similar to those of olmesartan and ZD7155 (Extended Data Fig. 7a,b). The only differences were observed in the orientation of the benzene and heterocyclic rings of Cpds **1** and **2**, which occupy the upper part of the ligand-binding pocket, beyond the interaction site of olmesartan and ZD7155. Similarly, docking into the $AT_2R$ structure suggested that ZD7155 and olmesartan can fit in the $AT_2R$ pocket, with their biphenyl-tetrazole scaffolds closely following the scaffolds of Cpds **1** and **2** in the corresponding $AT_2R$ crystal structures. Although docking supports binding of all four ligands in both $AT_1R$ and $AT_2R$ crystal structures, the binding scores of the ligands vary significantly, reflecting different

interactions of non-scaffold groups. The scores also qualitatively reflect differences in the affinities of these compounds, with the cognate ligands showing substantially better binding scores than the off-target binders.

## Mutagenesis of the ligand-binding pocket validates crystal structures

Point mutations were introduced in 17 residues of the $AT_2R$ ligand-binding pocket and their effects on ligand affinity were assessed for [3H]AngII peptide, as well as for the small molecule Cpds **1** and **2** in [3H]AngII competition assays (Supplementary Discussion and Extended Data Fig. 8).

Overall, the effects of mutations in the binding pocket of $AT_2R$ are consistent with the receptor-ligand interactions observed in the co-crystal structures with Cpds **1** and **2**. At the same time, most of these effects are distinct from the effects in $AT_1R$-sartan complexes, corroborating the substantial differences in the ligand binding modes between $AT_2R$ and $AT_1R$. Note that the effects of binding pocket mutations are practically identical for Cpds **1** and **2**, with the only notable exception of Trp269[6.48]Phe modestly (~5-fold) affecting affinity of Cpd **1**, but not of Cpd **2**.

## SAR provides further insights into receptor selectivity

The structure-activity relationship (SAR) of Cpd **1** analogs was studied using derivatization of the 3- (**R₁)** and 7- (**R₂**) positions of the quinazolinone core (Extended Data Table 2), and its structural basis was analyzed by molecular docking to the $AT_1R$ and $AT_2R$ crystal structures (Fig. 4). The SAR dataset comprised a series of 14 compounds spanning a wide range of selectivity for the two receptor types. Two members of the series were found to be highly selective for $AT_2R$ (530-fold for Cpd **1** and 410-fold for Cpd **3**), while two others showed a high degree of selectivity for $AT_1R$ (1,120-fold for Cpd **9** and 180-fold for Cpd **13**). The remaining compounds exhibited moderate (<15 fold) to no selectivity.

The SAR data showed that the **R₁** substituent is critical for high $AT_2R$ selectivity, while the **R₂** substituent mostly defines a high selectivity towards $AT_1R$ (Extended Data Table 2). Despite the dramatic differences in the pocket shapes and ligand-binding poses between $AT_2R$ and $AT_1R$, the docking results provide important insights into the structural basis of SAR observations and directions for optimization of $AT_2R$ selective ligands (see Supplementary Discussion).

## Conclusions

The two types of the AngII receptor are distinct in terms of their genetic variations, tissue specific expression, signaling, and regulation, as well as other physiological and pharmacological properties[1,47]. Although all of the conserved motifs of class A GPCRs are present in $AT_2R$, it exhibits an atypical behavior compared to other receptors[1]. Discerning the $AT_2R$-specific signaling pathways has been challenging and remains unresolved to date[4,5]. The features revealed in the $AT_2R$ structures reported here might provide potential explanations for its poor coupling to G proteins/β-arrestins. Based on our results, we hypothesize that helix VIII can play a dual role in the modulation of $AT_2R$ function. On the

one hand, upon adopting a conformation captured in the crystal structures, helix VIII may stabilize an active-like receptor state, while repressing canonical AT$_2$R activity in a self-inhibitory manner by sterically blocking the G protein/β-arrestin binding site. On the other hand, upon switching to a membrane-bound conformation helix VIII can support the recruitment of G proteins/β-arrestins for AT$_2$R signaling. Therefore, helix VIII may work as a gatekeeper for either suppression or activation of the receptor depending on its post-translational modifications and interactions with various receptor partners and its environment. This hypothesis is consistent with the previously observed failure of AT$_2$R to internalize, thus prolonging biological responses without desensitization[48,49]. Further investigation is needed to fully understand this phenomenon.

Both AngII receptors are important drug targets, since the blockade of AT$_1$R has anti-hypertensive effects, while the modulation of AT$_2$R could be useful for cardioprotection, neuropathic pain relief and treatment of a variety of other conditions. Designing molecules that selectively bind to a specific receptor type is often challenging but can be critical for different therapeutic purposes. Although the AT$_1$R and AT$_2$R ligands share common scaffolds, the ligand-binding pockets of these two receptors are strikingly different, and these differences could be exploited for designing selective ligands. The AT$_2$R crystal structures determined in this study improve our understanding of the two types of the human angiotensin receptors and provide new insights into the structural basis for the binding and selectivity of small molecules of therapeutic significance. Our results are therefore expected to facilitate the rational structure-based drug design for improved selectivity.

## METHODS

No statistical methods were used to predetermine sample size. The experiments were not randomized and the investigators were not blinded to allocation during experiments and outcome assessment.

### Protein engineering for structural studies

DNA encoding the human AT$_2$R (UNIPROT P50052) was synthesized by GenScript with optimization for expression in insect cells. The construct has truncations of the AT$_2$R residues 1–34 and 336–363. The thermostabilized apocytochrome $b_{562}$RIL (BRIL) from *E. coli* with mutations Met7Trp, His102Ile, and Arg106Leu was fused to the N-terminus of AT$_2$R, with a 4-residue linker (Gly-Ser-Gly-Ser). The BRIL-AT$_2$R chimera sequence was subcloned into vector **pFastBac1** (Invitrogen), with N-terminal haemagglutinin (HA) signal sequence, a FLAG tag, a 10×His tag, and a tobacco etch virus (TEV) protease cleavage site.

### Protein expression and purification

The BRIL-AT$_2$R protein was expressed in *Spodoptera frugiperda* (*Sf*9) insect cells (ATCC CRL-1711) using the Bac-to-Bac baculovirus expression system (Invitrogen). Cells were lysed by repeated washing and centrifugation, with hypotonic buffer (10 mM HEPES, pH 7.5, 10 mM MgCl$_2$, 20 mM KCl) and high osmotic buffer (10 mM HEPES, pH 7.5, 1.0 M NaCl, 10 mM MgCl$_2$, 20 mM KCl), adding EDTA-free complete protease inhibitor cocktail tablets (Roche). The washed membranes were suspended in hypotonic buffer with 2 mg/ml

iodoacetamide for 30 min at 4 °C, and then solubilized in 100 mM HEPES, pH 7.5, 800 mM NaCl, 0.5% (w/v) n-dodecyl-beta-D-maltopyranoside (DDM, Anatrace), 0.1% (w/v) cholesterol hemisuccinate (CHS, Sigma-Aldrich), and 10% (v/v) glycerol, for 4 hours at 4 °C. The solubilized BRIL-AT$_2$R protein was then bound to TALON IMAC resin (Clontech) overnight. The resin was washed with 10 column volumes of wash buffer I (50 mM HEPES, pH 7.5, 400 mM NaCl, 5% (v/v) glycerol, 0.1% (w/v) DDM, 0.02% (w/v) CHS, 10 mM imidazole), and 10 column volumes of wash buffer II (20 mM HEPES, pH 7.5, 200 mM NaCl, 5% (v/v) glycerol, 0.05% (w/v) DDM, 0.01% (w/v) CHS, 20 mM imidazole). The BRIL-AT$_2$R protein was eluted by 3 column volumes of elution buffer (20 mM HEPES, pH 7.5, 100 mM NaCl, 5% (v/v) glycerol, 0.02% (w/v) DDM, 0.004% (w/v) CHS, 300 mM imidazole), then incubated with 100 μM of ligand (Cpd **1** or **2**), treated overnight with TEV protease to remove tags, and concentrated to 15 mg/ml with a 100 kDa cutoff concentrator (Vivaspin). The protein yield and monodispersity were tested by analytical size exclusion chromatography (aSEC).

### Lipidic cubic phase crystallization

The AT$_2$R protein was reconstituted in lipidic cubic phase (LCP) by mixing the protein with monoolein supplemented with 10% cholesterol at a protein/lipid ratio of 2:3 (v/v) using a lipid syringe mixer. Crystallization trials were performed with an NT8-LCP robot (Formulatrix) in 96-well glass sandwich plates (Marienfeld) using 40 nL protein-loaded LCP and 800 nL precipitant solution per well. Plates were stored at 20 °C and imaged using a RockImager 1000 (Formulatrix). Crystals of AT$_2$R-Cpd **2** grew to an average size of 70×40×20 μm$^3$ within 21 days in 100 mM Tris-HCl, pH 8.0, 25–100 mM potassium formate, 25–35% (v/v) PEG400, and 0.3–1.2% (w/v) 1,6-hexanediol. Crystals were harvested using micromounts (MiTeGen) directly from LCP and flash-frozen in liquid nitrogen for diffraction data collection at the synchrotron radiation beamline. Micro-crystals of AT$_2$R-Cpd **1** for XFEL data collection were prepared by injecting 5 μl protein-laden LCP aliquots into 100 μl gas-tight syringes filled with 60 μl precipitant solution (100 mM Tris-HCl, pH 8.0, 25 mM potassium formate, 25% (v/v) PEG400, and 0.3% (v/v) (+/−)-2-Methyl-2,4-pentanediol). The crystals grew to an average size of 5×2×2 μm$^3$ within 5 days at 20 °C. Before loading the micro-crystals into the LCP injector, the excess precipitant solution was carefully removed from the syringes, and the remaining LCP with embedded crystals was consolidated together. Approximately 20% (v/v) 7.9 MAG was added and mixed with the LCP, to absorb the residual precipitant solution and prevent the formation of lamellar crystalline phase due to rapid evaporative cooling when injecting LCP into vacuum[34].

### Diffraction data collection using synchrotron radiation

Crystallographic diffraction data collection was performed at 23ID-D beamline (GM/CA) of the Advanced Photon Source in the Argonne National Laboratory. Diffraction data from 47 crystals of AT$_2$R-Cpd **2** were collected using a Pilatus3 6M detector with an unattenuated 10 μm minibeam (wavelength 1.0330 Å). Data were collected using 2 s exposure and 0.5° oscillation with the maximum wedge of 20° per crystal, and then integrated, scaled and merged using XDS[50].

## Diffraction data collection using X-ray free-electron laser

Serial Femtosecond Crystallography (SFX) data collection was performed using the CXI instrument at the Linac Coherent Light Source (LCLS) at SLAC National Accelerator Laboratory. The LCLS was operated at a wavelength of 1.3 Å (9.57 keV) delivering individual X-ray pulses of 40 fs pulse duration and ~$10^{11}$ photons per pulse focused into a spot size of approximately 1.5 μm in diameter using a pair of Kirkpatrick-Baez mirrors. Microcrystals of $AT_2R$-Cpd **1** were delivered in the LCP media using a microextrusion injector[34] with 50 μm nozzle running at ~220 nL/min flow rate. Diffraction images were recorded at a rate of 7,200 patterns per minute (120 Hz) with the 2.3 Megapixel Cornell-SLAC Pixel Array Detector (CSPAD). A total of 2,701,530 images were collected, 175,241 of which were identified as hits with the Cheetah program (6.5% hit rate). Surprisingly, indexing revealed two different lattices, monoclinic and orthorhombic, apparently belonging to different microcrystals of $AT_2R$-Cpd **1** co-existing in the same crystallization batch. Therefore, 22,774 hits were successfully indexed in a *2/m* Laue group and 15,804 hits in a *mmm* Laue group with different lattice parameters. Both datasets were merged separately using the standard CrystFEL pipeline[51] of Monte Carlo averaging without additional scaling step applying per-pattern resolution cutoff with '*pushres* 1.2' option.

## Structure determination

The structure was initially solved using molecular replacement (MR) with the monoclinic data sets collected at XFEL and synchrotron source. MR models for $AT_2R$ were produced by alignment of $AT_2R$ sequence with sequences of previously solved GPCRs. The top 20 templates were further edited to preserve the conserved residues and trim non-conserved residues to alanines. MR search with Phaser[52] identified locations of two receptors in asymmetric unit with a TFZ > 9. Further MR search with fixed positions of the two receptors using PDB ID 1MT6 as the search model for BRIL found one BRIL molecule in the asymmetric unit. Refinements and model completion were performed by repetitive cycling between Refmac5 and autoBUSTER, followed by manual examination and rebuilding of the refined coordinates in Coot[53], using both 2mFo-DFc and mFo-DFc maps, as well as omit maps calculated using Bhat's procedure[54]. The second BRIL molecule was modeled manually in the available electron density when Rfree dropped below 0.33. The final data collection and refinement statistics are shown in Extended Data Table 1. The Ramachandran statistics determined by MolProbity[55] are as follows: 96.8% in favored region, 3.2% allowed, 0 outlier for monoclinic $AT_2R$-Cpd **1**; 97.6% in favored region, 2.4% allowed, 0 outlier for orthorombic $AT_2R$-Cpd **1**; 97.4% in favored region, 2.6% allowed, 0 outlier for $AT_2R$-Cpd **2**.

## Docking simulations

$AT_1R$ and $AT_2R$ selective and non-selective ligands were docked into the $AT_1R$ and $AT_2R$ crystal structures, $AT_1R$ active-like state and $AT_2R$ inactive state models using an energy-based docking protocol implemented in ICM molecular modeling software (Molsoft, LLC). The structures of the receptors were protonated and optimized using an ICM docking pipeline. The active and inactive state receptor models were obtained using homology modeling algorithm implemented in ICM. Crystal structures of $AT_2R$ and $AT_1R$ were used

as templates for the $AT_1R$ active-like state model and the $AT_2R$ inactive state model, respectively. Molecular models of the compounds were generated from two-dimensional representations and their 3D geometry was optimized using MMFF-94 force field[56]. Molecular docking employed biased probability Monte Carlo (BPMC) optimization of the ligand internal coordinates in the grid potentials of the receptor[57]. To ensure exhaustive sampling of the ligand binding pose parameter thoroughness was set to 30 and at least five independent docking runs were performed for each ligand starting from a random conformation. The results of individual docking runs for each ligand were considered consistent if at least three of the five docking runs produced similar ligand conformations (RMSD < 2.0 Å) and binding score < −25.0 kJ/mol. The unbiased docking procedure did not use distance restraints or any other a priori derived information for the ligand-receptor interactions.

## Molecular dynamics

The initial receptor coordinates were derived from the $AT_2R$ crystal structures in complexes with Cpd **1** and Cpd **2**. The N-terminal fusion partner BRIL was removed and the terminal amino acids Cys35 and Arg337 were acetylated and amidated, respectively. We used ICM-Pro package (www.molsoft.com) to construct the model in the regions of missing electron densities for side chains and especially for the intracellular loop (ICL) regions. The orientations of $AT_2R$ in the apo and the ligand bound models were aligned to $AT_1R$ orientation in the membrane taken from the OPM database (www.opm.phar.umich.edu).

Initial ligand parameterization was performed in CGenFF available with CHARMM-GUI interface[58]. For corrections in charge assignments with high penalty values, Cpd **1** and Cpd **2** were fragmented and re-parameterized using Gaussian03 package and Force Field Tool-Kit available with VMD v.1.9.2[59]. CHARMM36 additive force field was used for rest of the system[60]. We used homogenous lipid bilayer of 164 palmitoyloleoylphosphatidylcholine (POPC) lipids. TIP3P water model used for solvation of the lipids-receptor-ligand system with 150 mM salt concentration of $Na^+$ and $Cl^-$.

The initial input files generated using CHARMM-GUI interface were simulated using GROMACS v5.0.4 molecular simulation package compiled to run in parallel computing architecture using multiple GPUs [61]. Each simulation was performed on a cluster of 4 nodes connected via InfiniBand, where a single node had 16 Intel Xeon 2.4 GHz processors and 2 NVIDIA Tesla K20 GPUs. Simulation parameters include a 1 fs (femtosecond) time step for the first step of the equilibration, followed by a 2 fs time step for the rest of the equilibration and production simulations. During initial phase of NVT ensemble, temperature was set at 310 K using Berendsen thermostat[62], and the initial harmonic restraints of 10.0 kCal /mol/Å$^2$ applied for protein and lipid heavy atoms. These restraints were gradually reduced throughout the equilibration phase, followed by a production phase with no restraints. In the production phase of NPT ensemble, the pressure was set to 1 bar using Parrinello-Rahman barostat and 310 K temperature with Nose-Hoover thermostat. Non-bonded interaction calculations cut-off was set at 12 Å. The Particle mesh Ewald (PME) FFT grid was used with a dimension of 64×64×96 for all simulations. Bond lengths to H-atoms were constrained using P-LINCS algorithm[63].

A total of 10.2 μs of production MD simulation were performed to study the interactions of Helix VIII in $AT_2R$, including 8 runs of 0.5 μs each for crystal structure starting conformations, $8 \times 0.25$ μs for perturbed position of helix VIII, and $6 \times 0.7$ μs for $AT_1R$-like starting conformation of helix VIII. Simulation trajectories were analyzed using GROMACS and VMD[59]. Plots and images were generated using Grace (http://plasma-gate.weizmann.ac.il/Grace) and ICM-Pro.

### Radioligand binding assays

Radioligand binding studies were performed using mammalian virus-like particles (VLPs) containing wild-type $AT_1R$, wild-type $AT_2R$, or the engineered BRIL-$AT_2R$. VLPs were produced using the Expi293 MembranePro Expression System (ThermoFisher) per the manufacturer's instructions. Total protein concentration was determined by Bradford assay. VLPs were re-suspended in cold Dulbecco's Phosphate-Buffered Saline (PBS) without calcium or magnesium (Gibco). Aliquots were flash-frozen and stored at −80 °C. All binding reactions were carried out in 96-well microplates (Corning). The assay buffer (50 μL) consisted of 20 mM HEPES pH 7.4, 5 mM $MgCl_2$, 1 mM EDTA, and 0.005 % Tween-20. Non-specific binding was determined in the presence of 1 μM AngII. Final concentrations of $[^{125}I]$-Sar$^1$-Ile$^8$-AngII (Perkin Elmer) were typically 0.05–5 nM in saturation and 0.3 nM in competition binding experiments. For both types of assays, 37.5 ng (wild-type $AT_1R$ or engineered BRIL-$AT_2R$) or 13.5 ng (wild-type $AT_2R$) VLPs were used per well. Competing ligands were added as DMSO solutions, resulting in a total organic solvent content of 1 %. Reactions were incubated for 3 hours at room temperature. Bound ligand was separated from free ligand by processing 25 μL of each reaction mixture on 96-well Zeba Spin desalting plates with a molecular weight cut-off of 40 kDa (ThermoScientific) according to the manufacturer's instructions. Eluates were collected in isoplates-96 microplates by centrifugation ($100 \times g$ for 3 min) and bound ligand was quantitated after addition of 150 μL of UltimaGold MV scintillation fluid on a Perkin Elmer Wallac Microbeta TriLux 1450 scintillation counter. All reagent transfers were conducted using a Hamilton liquid handler. Data were analyzed by non-linear curve-fitting using the program GraphPad Prism 6. Binding data is reported as mean ± s.e.m.

### Mutagenesis of the ligand-binding pocket residues and radioligand binding assays

Radioligand binding assays were performed as previously described[25]. Briefly, ligand binding was measured using washed membranes from HEK 293 cells (FreeStyle™ 293-F, ThermoFisher, cat. R79007) transiently expressing WT $AT_2R$ or point mutant $AT_2R$ constructs. Cells were lysed in buffer (25 mM HEPES, pH 7.5) with protease inhibitor cocktail consisting of AEBSF (GoldBio), E-64, Leupeptin, Aprotinin (AGScientific), and dounce homogenized. Membranes were centrifuged for 15 minutes at $30,000 \times g$. Total protein concentration was measured by Bradford assay, and membrane pellets were frozen in liquid nitrogen and stored at −80 °C. Binding assays were carried out in a total volume of 0.25 mL in 96-well plates with a binding buffer (140 mM NaCl, 5 mM KCl, 1mM EDTA, 25 mM HEPES, pH 7.4, 0.006% BSA) containing 1 nM $[^3H]$AngII (American Radiolabeled Chemicals, Inc) for 60 minutes at room temperature. Membranes were harvested over 0.3% polyethyleneimine-treated, 96-well filter mats using a 96-well Filtermate harvester (Perkin Elmer) and washed 3 times with cold buffer (25 mM HEPES, pH 7.5). Filter mats were

dried, wax scintillant was melted onto each filter, and radioactivity was counted in a MicroBeta2 TriLux plate scintillation counter (Perkin Elmer). AngII $K_d$ for WT and mutants were determined using homologous competition binding. $K_i$ was determined using [$^3$H]AngII competition with 12 concentrations of unlabeled ligand (10,000 uM – 0.01 nM). The data were analyzed by Prism 6.05 (GraphPad Software) to give $K_d$ and $K_i$ values and reported as the mean ± s.e.m.

## Compound preparation

All molecules presented in this manuscript were prepared according to the appropriate literature and/or patent publications: Compounds **1**, **3** (ref. 26), Compounds **2**, **5**, **6**, **10**, **12**, and **14** (ref. 27), Compounds **4** and **11** (ref. 64), Compounds **7–9** (ref. 65), Compound **13** (ref. 66).

## Cell lines

Sf9 cells were purchased from the American Type Culture Collection. HEK 293 cells were acquired from ThermoFisher. The cell lines have not been authenticated. All cell lines have been tested and shown to be free from mycoplasma.

## Data availability

Atomic coordinates and structure factors for the AT$_2$R-Cpd **1**, monoclinic and orthorhombic, and AT$_2$R-Cpd **2** structures have been deposited into the Protein Data Bank with accession codes 5UNF, 5UNG, and 5UNH, respectively. All other data are available from the corresponding authors upon reasonable request.
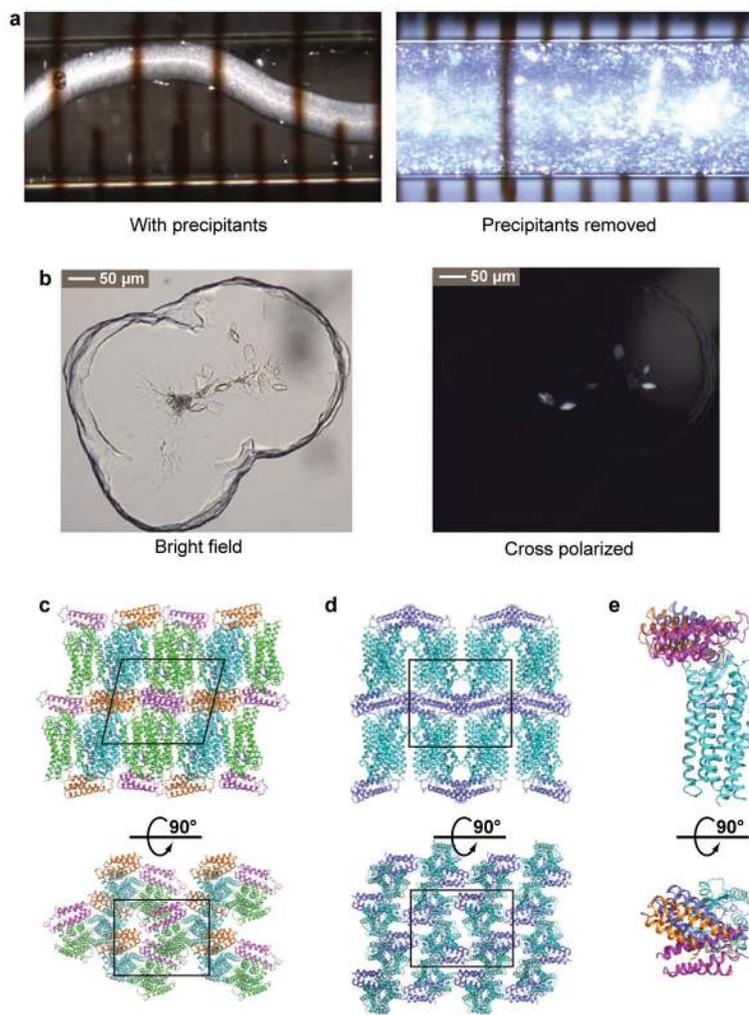
## Extended Data
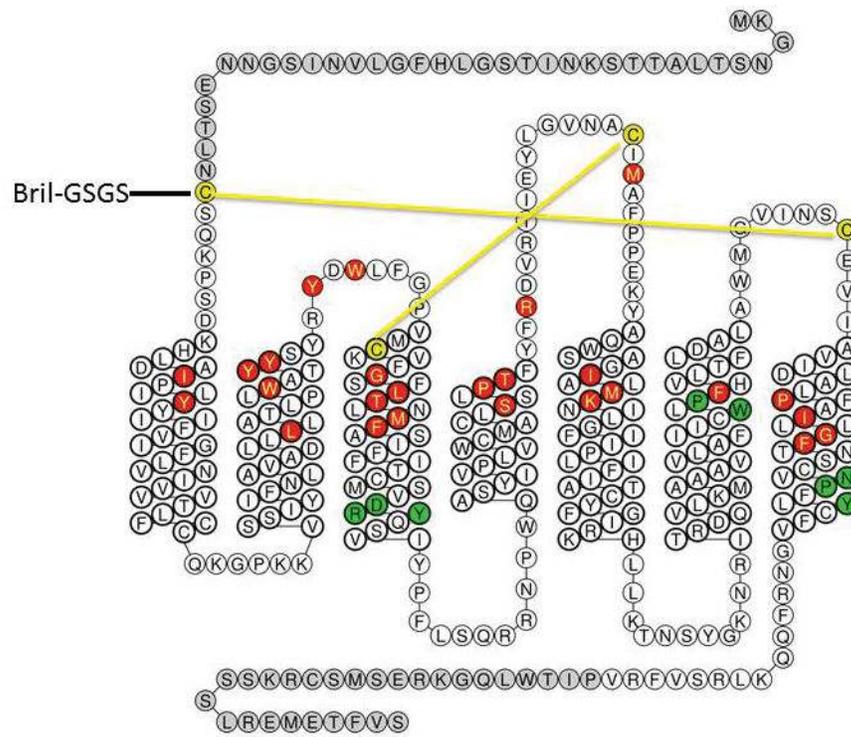


**Extended Data Figure 1. AT₂R "snake" diagram and protein engineering**

Truncations are shown in grey, disulfide bonds in yellow, ligand-binding residues in red, conserved motifs in green.
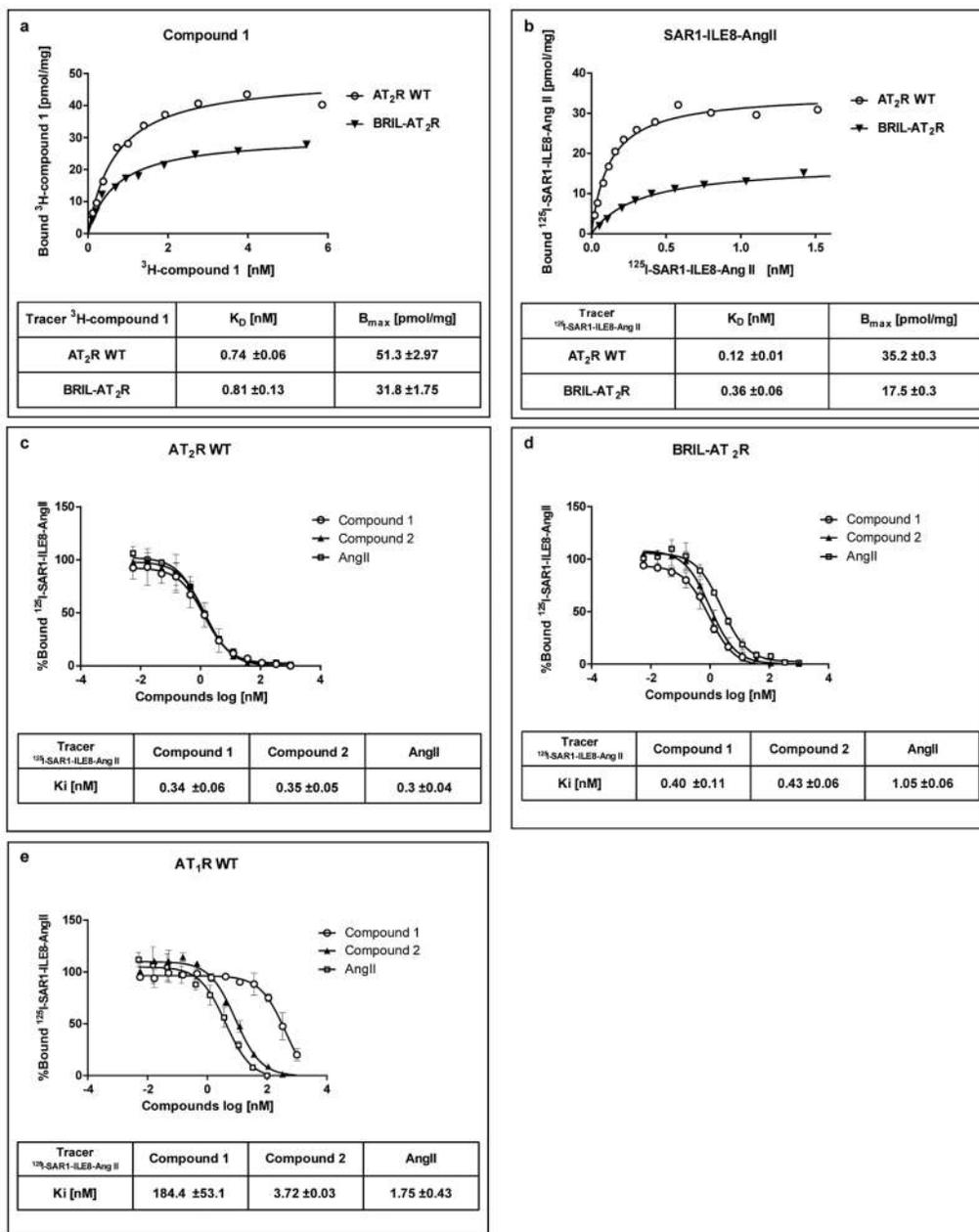
**Extended Data Figure 2. Radioligand binding assays**

**a, b,** Saturation binding of Cpd **1** and Sar[1]-Ile[8]-AngII. Specific binding of [^{3}H]-Cpd **1** (a) and [^{125}I]-Sar[1]-Ile[8]-AngII (b) to the wild-type (open circle) and engineered $AT_2R$ (closed triangle), representative of two separate experiments; **c–e,** Competition binding of Cpd **1** (open circle), Cpd **2** (closed triangle) and AngII (open square) to the wild-type $AT_2R$ (**c**), engineered $AT_2R$ (**d**) and wild type $AT_1R$ (**e**) with [^{125}I]-Sar[1]-Ile[8]-AngII as a tracer; each point represents the mean ± s.e.m. of two separate experiments, each performed in duplicates.

**Extended Data Figure 3. Crystallization of AT$_2$R and crystal packing**

**a,** AT$_2$R-Cpd **1** crystals grown in a syringe for XFEL data collection. **b,** AT$_2$R-Cpd **2** crystals grown in a glass sandwich plate for synchrotron data collection. **c,** Crystal packing in the monoclinic space group (AT$_2$R-Cpd **1** and AT$_2$R-Cpd **2** structures), side and top views (AT$_2$R in green and cyan; BRIL in orange and pink). **d,** Crystal packing in the orthorhombic space group (AT$_2$R-Cpd **1** structure), side and top views (AT$_2$R in cyan; BRIL in blue). **e,** Different BRIL orientations in the two BRIL-AT$_2$R molecules in the asymmetric unit of monoclinic AT$_2$R-Cpd **1** structure and AT$_2$R-Cpd **2** structure (pink and orange), and in the orthorhombic AT$_2$R-Cpd **1** structure (blue) with AT$_2$R in cyan, side and top views. Unit cell in (**c**) and (**d**) is outlined in black line.
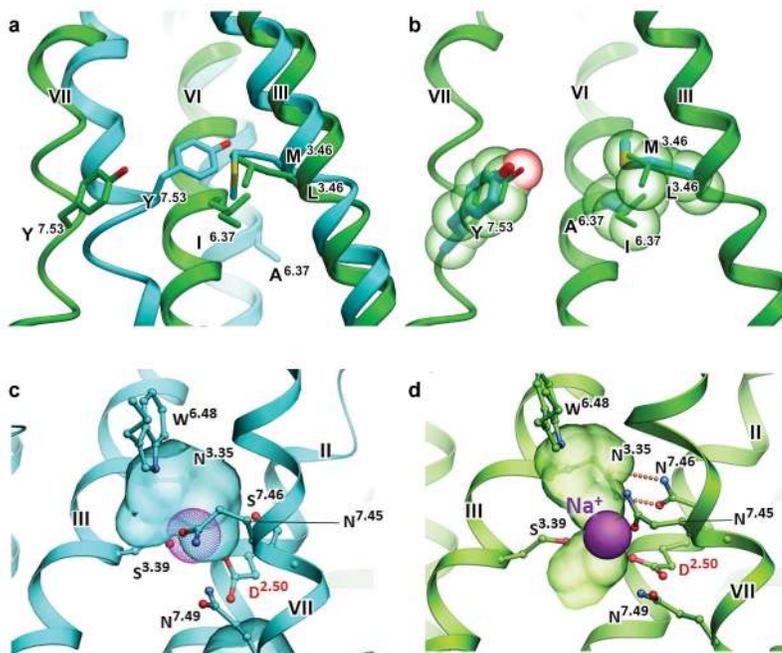
**Extended Data Figure 4. Conserved L[M]$^{3.46}$ – I[A]$^{6.37}$ – Y[Y]$^{7.53}$ microswitch and sodium binding pocket in AT$_1$R and AT$_2$R**

**a,** Comparison of the conserved residue triad between AT$_1$R (green, PDB 4YAY) and AT$_2$R (cyan) structures, shows a rearrangement of interactions consistent with AT$_2$R activation. **b,** Modeling of the AT$_2$R in a hypothetical inactive state (cyan), based on the AT$_1$R crystal structure template (green) shows that replacement of a large hydrophobic residue in position 6.37, as conserved in most class A GPCRs, to a rare small Ala258$^{6.37}$ in AT$_2$R drastically reduces the hydrophobic contact in this region between helices III and VI in the inactive state. **c,d,** Sodium binding pocket in AT$_2$R (**c**) and AT$_1$R (PDB 4YAY) (**d**) is shown as a surface with hydrogen bonds between Asn$^{7.46}$ and Asn$^{3.35}$ as orange spheres. Putative sodium ion in the AT$_1$R structure (**d**) is shown as a solid magenta sphere, while the same position in the AT$_2$R structure (**c**) is marked as a dotted sphere. Potential sodium-coordinating residues are shown as sticks.
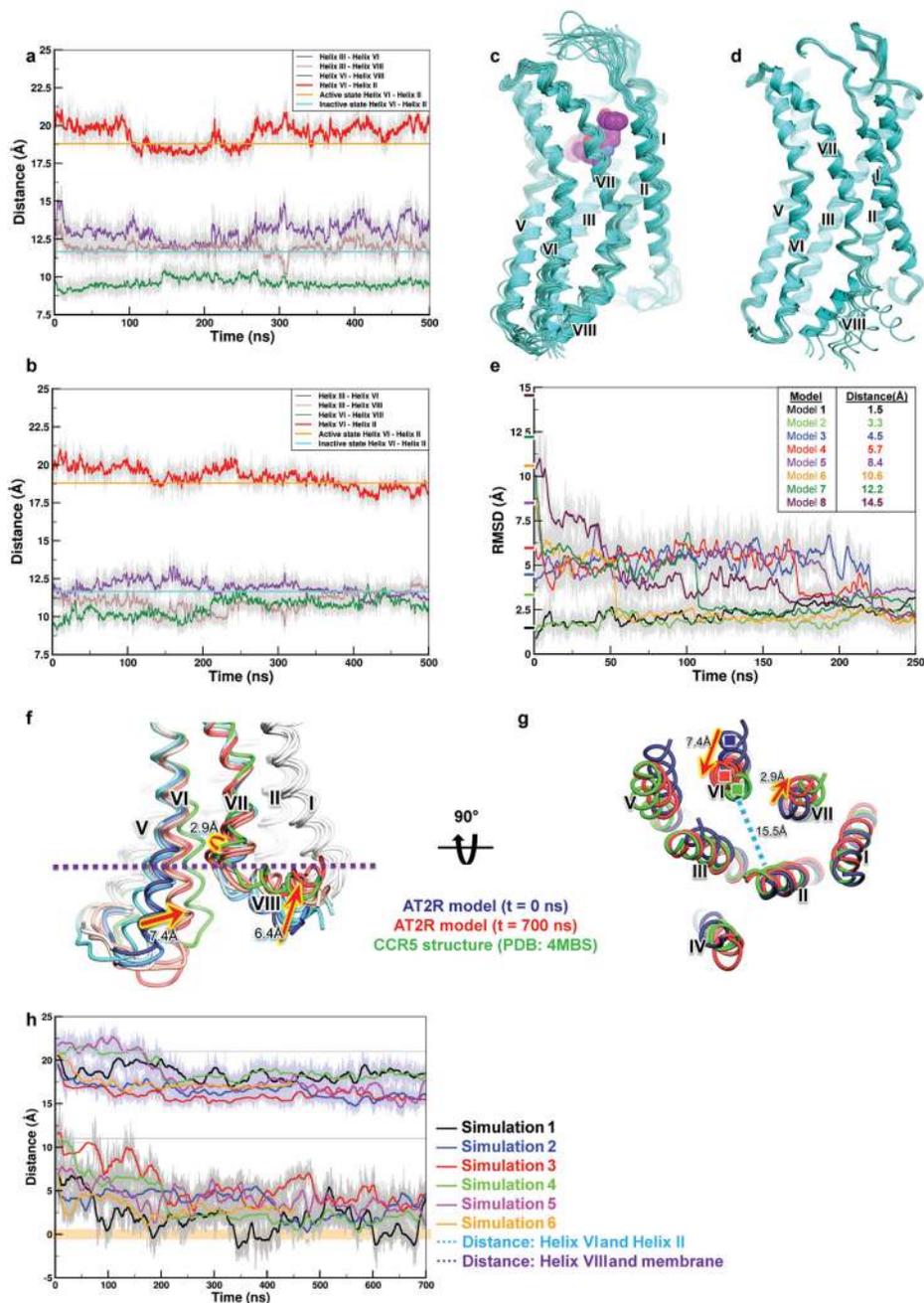
**Extended Data Figure 5. Summary of MD simulations**

**a–c,** Conformational stability of $AT_2R$ structure is illustrated by representative conformations from a total of 4 μs of MD simulations (eight independent 500 ns runs), clustered by RMSD. Traces of distances measured between different helices are shown for apo $AT_2R$ (**a**) and for the $AT_2R$-Cpd **1** complex (**b**). Distances were calculated between the centers of mass of residues $Ser79^{2.39}$-$Ile83^{2.43}$ for helix II, $Arg142^{3.50}$-$Val146^{3.54}$ for helix III, $Gln253^{6.32}$-$Met257^{6.36}$ for helix VI, and Phe325-Lys328 for helix VIII. **d,e,** Conformational stability of helix VIII upon perturbations, using eight starting conformations

of helix VIII (**d**) is revealed by RMSD traces (**e**), which all converge by ~250 ns of simulations. RMSD values are calculated for the center of mass of Cα atoms of residues Phe325-Lys328 compared to the crystal structure of $AT_2R$. Tick marks on the Y-axis show the starting frame RMSD values. Colored lines are plotted using values averaged over a 500 ps window. **f–h,** Results of MD simulations for a modified $AT_2R$ model with the backbone of helix VIII aligned with helix VIII from $AT_1R$ structure (PDB 4YAY). Conformational snapshots of the $AT_2R$ model (**f**) are shown for every 100 ns (blue to red spectrum) from one of the six independent 700 ns MD simulation runs (simulation 5). Green cartoon shows inactive-state conformation of CCR5 (PDB 4MBS), helix VIII of which was found to be the closest to the final conformations of $AT_2R$ helix VIII in MD simulations. Intracellular view (**g**) of snapshots from the same MD simulation is shown only t=0 and t=700 ns. Traces of the distance between helices VI and II (**e**, upper curves), calculated between the centers of mass of Cα atoms of residues $Gln253^{6.32}$-$Met257^{6.36}$ in helix VI and residues $Ser79^{2.39}$-$Ile83^{2.43}$ in helix II, show a change from 21 Å (active state) to under 16 Å (inactive state). Traces of the distance between helix VIII and membrane (**e**, lower curves), calculated between the center of mass of Cα atoms of residues R330–V332 and the closest phosphate atoms of lipid molecules, indicate a gradual shift of helix VIII towards the lipid bilayer, with the distance decreasing from ~10 Å to under 3 Å.
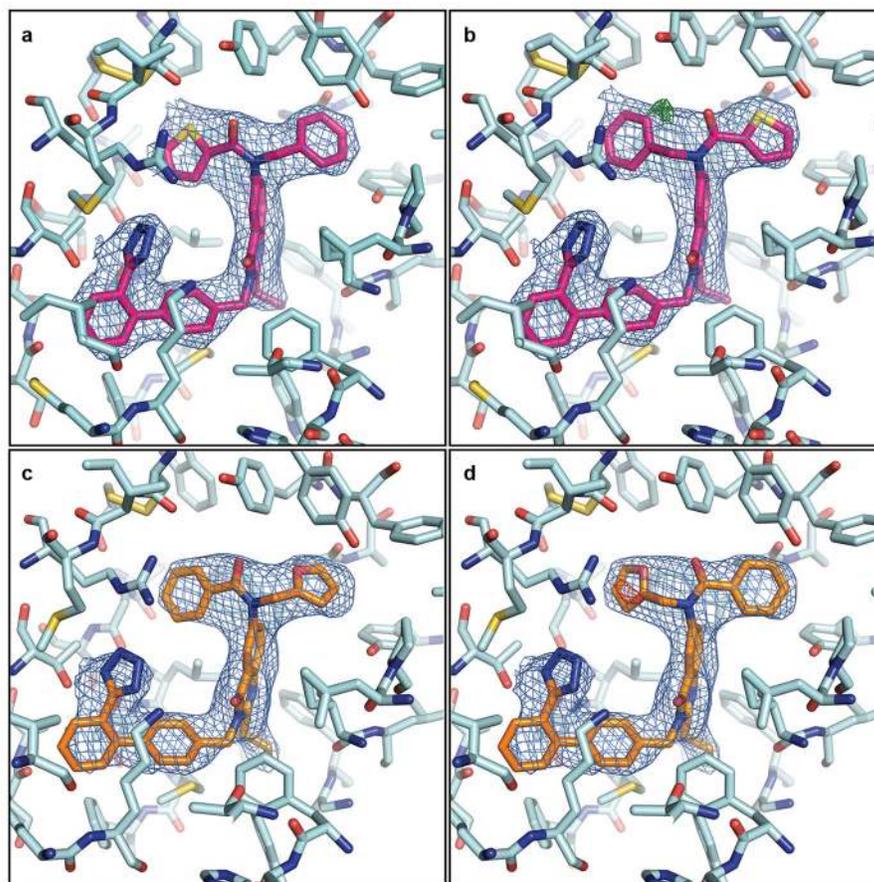


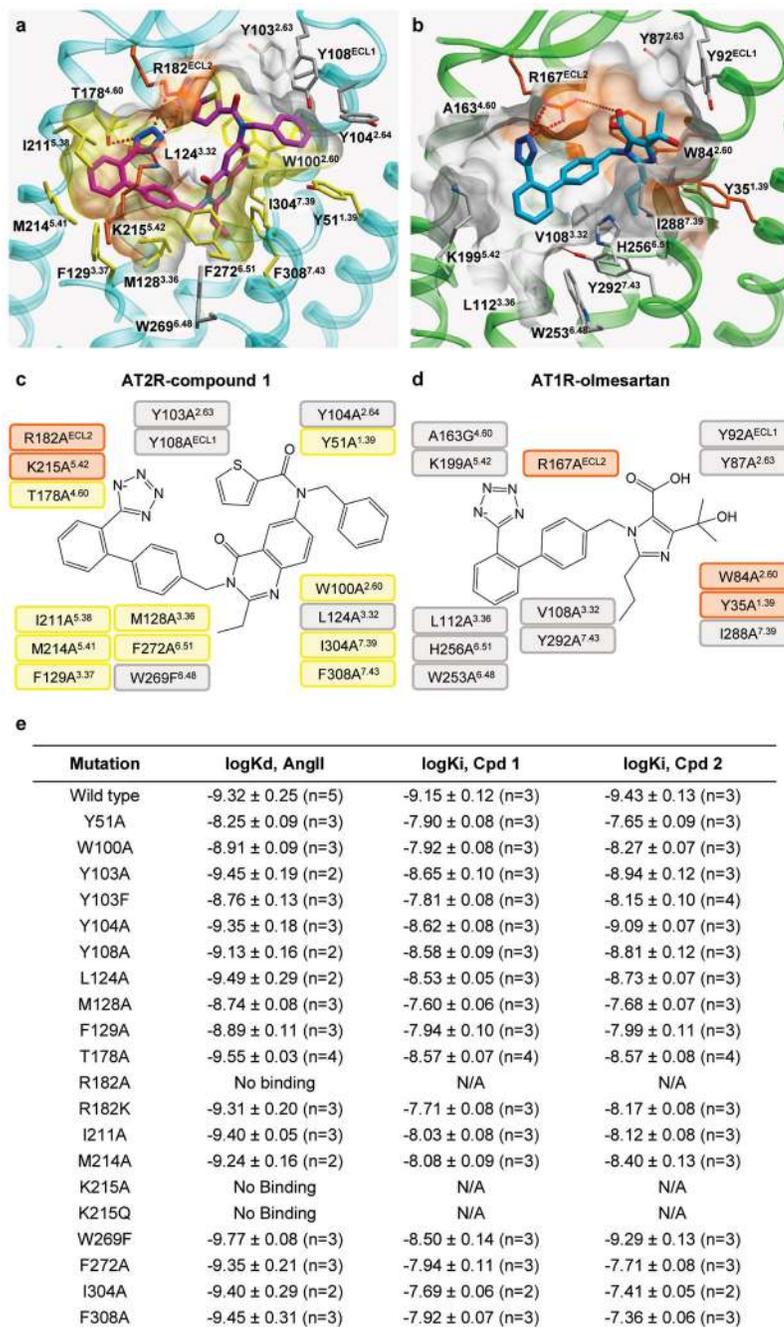**Extended Data Figure 6. Electron density for Cpd 1 and Cpd 2**

**a, b,** Cpd **1** can be modeled in two possible conformations, (**a**) and (**b**), with alternative orientations of the benzene and thiophene rings. **c, d,** Cpd **2** can be modeled in two possible conformations, (**c**) and (**d**), with alternative orientations of the benzene and furan rings. 2mFo-DFc electron density (blue mesh) for Cpd **1** contoured at 1 σ, and mFo-DFc density (green mesh – positive, red mesh – negative) contoured at 3 σ. The conformations shown in panels (**a**) and (**c**) were used in the final crystal structures because of a slightly better ligand fit and the absence of strong difference mFo-DFc density. Both conformations for each ligand, however, are possible and indistinguishable by docking studies.
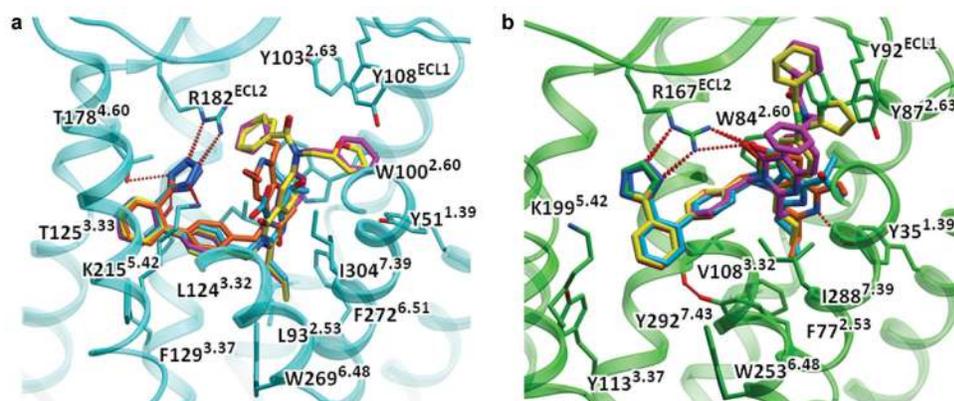


| Compound | AT$_1$R K$_i$ nM | AT$_2$R K$_i$ nM | AT$_1$R, inactive, docking score, kJ/mol | AT$_1$R, active, docking score, kJ/mol | AT$_2$R, active, docking score, kJ/mol | AT$_2$R, inactive, docking score, kJ/mol |
|---|---|---|---|---|---|---|
| Cpd **1** | 180 | **0.34** | -30 | -21 | **-44** | -39 |
| Cpd **2** | 3.7 | **0.35** | -33 | N/B | **-43** | -41 |
| Olmesartan | **5.3** | N/A | -33 | N/B | -27 | -31 |
| ZD7155 | **3.0** | N/A | -36 | -19 | -19 | -19 |

N/A – data not available
N/B – no binding observed

**Extended Data Figure 7. Ligand binding and cross-docking in AT$_2$R and AT$_1$R structures**
**a,b,** Docking poses of Cpd **1** (magenta), Cpd **2** (yellow), olmesartan (blue) and ZD7155 (orange) in the crystal structures of AT$_2$R (**a**) and AT$_1$R (**b**). Receptors are shown in carton representation, ligands are shown as sticks, and hydrogen bonds/salt bridges are shown as dashed lines. **c,** Ligand binding affinities and docking scores for AT$_2$R and AT$_1$R ligands. Data for the cognate ligands are shown in bold. Inactive state AT$_1$R and active-like state of AT$_2$R correspond to crystal structures. Active-like state of AT$_1$R and inactive state of AT$_2$R were modeled based on the crystal structures of AT$_2$R and AT$_1$R, respectively.

| Mutation | logKd, AngII | logKi, Cpd 1 | logKi, Cpd 2 |
|---|---|---|---|
| Wild type | -9.32 ± 0.25 (n=5) | -9.15 ± 0.12 (n=3) | -9.43 ± 0.13 (n=3) |
| Y51A | -8.25 ± 0.09 (n=3) | -7.90 ± 0.08 (n=3) | -7.65 ± 0.09 (n=3) |
| W100A | -8.91 ± 0.09 (n=3) | -7.92 ± 0.08 (n=3) | -8.27 ± 0.07 (n=3) |
| Y103A | -9.45 ± 0.19 (n=2) | -8.65 ± 0.10 (n=3) | -8.94 ± 0.12 (n=3) |
| Y103F | -8.76 ± 0.13 (n=3) | -7.81 ± 0.08 (n=3) | -8.15 ± 0.10 (n=4) |
| Y104A | -9.35 ± 0.18 (n=3) | -8.62 ± 0.08 (n=3) | -9.09 ± 0.07 (n=3) |
| Y108A | -9.13 ± 0.16 (n=2) | -8.58 ± 0.09 (n=3) | -8.81 ± 0.12 (n=3) |
| L124A | -9.49 ± 0.29 (n=2) | -8.53 ± 0.05 (n=3) | -8.73 ± 0.07 (n=3) |
| M128A | -8.74 ± 0.08 (n=3) | -7.60 ± 0.06 (n=3) | -7.68 ± 0.07 (n=3) |
| F129A | -8.89 ± 0.11 (n=3) | -7.94 ± 0.10 (n=3) | -7.99 ± 0.11 (n=3) |
| T178A | -9.55 ± 0.03 (n=4) | -8.57 ± 0.07 (n=4) | -8.57 ± 0.08 (n=4) |
| R182A | No binding | N/A | N/A |
| R182K | -9.31 ± 0.20 (n=3) | -7.71 ± 0.08 (n=3) | -8.17 ± 0.08 (n=3) |
| I211A | -9.40 ± 0.05 (n=3) | -8.03 ± 0.08 (n=3) | -8.12 ± 0.08 (n=3) |
| M214A | -9.24 ± 0.16 (n=2) | -8.08 ± 0.09 (n=3) | -8.40 ± 0.13 (n=3) |
| K215A | No Binding | N/A | N/A |
| K215Q | No Binding | N/A | N/A |
| W269F | -9.77 ± 0.08 (n=3) | -8.50 ± 0.14 (n=3) | -9.29 ± 0.13 (n=3) |
| F272A | -9.35 ± 0.21 (n=3) | -7.94 ± 0.11 (n=3) | -7.71 ± 0.08 (n=3) |
| I304A | -9.40 ± 0.29 (n=2) | -7.69 ± 0.06 (n=2) | -7.41 ± 0.05 (n=2) |
| F308A | -9.45 ± 0.31 (n=3) | -7.92 ± 0.07 (n=3) | -7.36 ± 0.06 (n=3) |

**Extended Data Figure 8. Mutagenesis of the AT$_2$R ligand-binding pocket**
**a,** Ligand-binding pocket from the AT$_2$R-Cpd **1** crystal structure. **b,** Ligand-binding pocket from the AT$_1$R-olmesartan crystal structure. **c,** Schematics of interactions between Cpd **1** and AT$_2$R residues. **d,** Schematics of interactions between olmesartan and AT$_1$R residues. In all panels, residues are colored according to their effect on affinity: more than 100-fold decrease in affinity (orange); 5–100-fold decrease in affinity (yellow); less than 5-fold decrease in affinity (grey). **e,** Effects of single residue mutations in the AT$_2$R ligand-binding

pocket on the ligand binding affinities. Values represent mean ± s.e.m. with the number of experiments shown in parenthesis.

### Extended Data Table 1

Data collection and refinement statistics (molecular replacement).

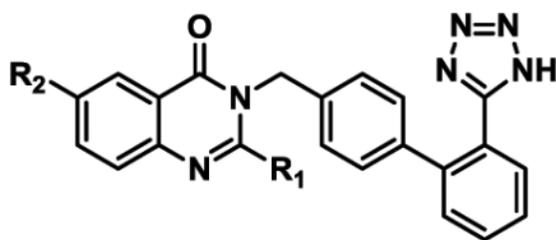| | AT$_2$R-Cpd 1 (XFEL) | | AT$_2$R-Cpd 2 (Synchrotron) | |
|---|---|---|---|---|
| Space group | P2$_1$ | P2$_1$22$_1$ | P2$_1$ | |
| Unit cell parameters | | | | |
| *a,b,c* (Å) | 77.4,69.1,90.1 | 70.3, 78.8, 93.4 | 78.4,68.2, 89.1 | |
| α,β,γ (°) | 90.0, 104.3, 90.0 | 90.0, 90.0, 90.0 | 90.0, 104.3, 90.0 | |
| **Data collection** | | | | |
| Number of collected frames | 2,701,530 | 2,701,530 | *N.A..* | |
| Number of hits/indexed images | 175,241/22,774 | 175,241/15,804 | *N.A..* | |
| Number of total/unique reflections | 1,412,692/22,934 | 1,139,069/13,330 | 64,806/18,479 | |
| Resolution (Å) | 30-2.8 (2.9-2.8)[#] | 30-2.8 (2.9-2.8) | 47.30-2.9 (3.06-2.90) | |
| Completeness (%) | 100(100) | 100(100) | 91.0(83.2) | |
| Multiplicity | 61.6(16.3) | 85.5 (27.2) | 3.5 (2.5) | |
| *I/σ(I)* | 4.1 (0.8) | 4.9(1.0) | 5.8(1.8) | |
| *CC** | 0.98 (0.24) | 0.99 (0.36) | 0.99 (0.84) | |
| $R_{split}$ Or $R_{merge}$(%) | 16.4(172) | 14.8(124) | 12.5 (44.2) | |
| **Refinement** | | | | |
| Resolution (Å) | 29.57-2.80 | 28.96-2.80 | 30.00-2.90 | |
| Number of reflections/test set | 22,906/1,118 | 13,269/691 | 18,462/906 | |
| $R_{work}$/$R_{free}$ | 0.227/0.256 | 0.241/0.262 | 0.216/0.259 | |
| Number of atoms | | | | |
| | A | B | A | B |
| Receptor/BRIL | 3,103 | 3,048 / 3,195 | 2,983 | 2,800 |
| Ligand | 46 | 46 / 46 | 47 | 47 |
| Lipid and other | 0 | 0 / 25 | 0 | 0 |
| Wilson *B*-factors (Å$^2$) | 90.8 | 80.9 | 79.1 | |
| Mean overall *B* value (Å$^2$) | | | | |
| | A | B | A | B |
| Receptor | 131.5 | 84.6 / 82.1 | 72.0 | 114.2 |
| BRIL | 141.7 | 107.8 / 86.1 | 106.1 | 138.6 |
| Ligand | 126.5 | 64.2 / 63.8 | 62.1 | 112.7 |
| Lipid and other | - | - / 82.6 | - | - |
| R.m.s bonds (Å)/angles (°) | 0.010/0.90 | 0.009/0.92 | 0.009/0.97 | |

Data collected from 47 crystals were used for the AT$_2$R-Cpd **2** structure determination.

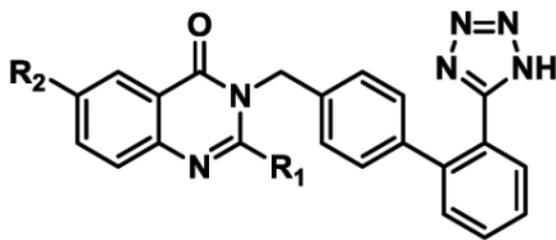[#]Numbers in parentheses represent values from the highest resolution shell.

## Extended Data Table 2

SAR for quinazolinone-biphenyltetrazole derivatives in $AT_2R$ and $AT_1R$.
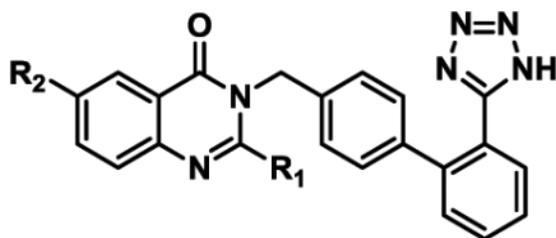


| Compound | $R_1$ | $R_2$ | $AT_2R$ $K_i$(nM)[*] | $AT_2R$ $K_i$(nM)[*] | $AT_2R$ fold selectivity |
|---|---|---|---|---|---|
| 1 | Ethyl |  | 0.34 ± 0.06 | 184 ± 50 | 530x |
| 2 | n-Propyl |  | 0.35 ± 0.05 | 3.72 ± 0.03 | 11x |
| 3 | Methyl |  | 1.7 ± 0.4 | 700 ± 200 | 410x |
| 4 | n-Propyl |  | 0.65 ± 0.01 | 1.8 ± 0.2 | 2.8x |
| 5 |  |  | 11.5 ± 0.5 | 37 ± 3 | 3.2x |
| 6 |  |  | 120 ± 50 | 450 ± 20 | 3.8x |

| Compound | $R_1$ | $R_2$ | AT$_2$R K$_i$(nM)[*] | AT$_2$R K$_i$(nM)[*] | AT$_2$R fold selectivity |
|---|---|---|---|---|---|
| 7 | *n*-Propyl | | 1.7 ± 0.5 | 10.4 ± 1.7 | 6.1x |
| 8 | *n*-Propyl | | 10.9 ± 0.1 | 9.90 ± 0.01 | 0.9x |
| 9 | *n*-Propyl | | 1,790 ± 150 | 1.6 ± 0.1 | 0.001x |
| 10 | *n*-Propyl | | 4.9 ± 0.2 | 12.9 ± 2.8 | 2.6x |
| 11 | *n*-Propyl | | 4.1 ±0.8 | 6.7 ± 0.9 | 1.6x |
| 12 | *n*-Propyl | | 18.8 ± 0.1 | 17.3 ± 4.3 | 0.9x |
| 13 | *n*-Propyl | | 2,990 ± 80 | 16.7 ± 10.4 | 0.006x |

| Compound | R₁ | R₂ | AT₂R Kᵢ(nM)* | AT₂R Kᵢ(nM)* | AT₂R fold selectivity |
|---|---|---|---|---|---|
| **14** | **Methyl** | | $5,300 \pm 2,400$ | $360 \pm 80$ | 0.07x |

*Competition binding assay with $[^{125}I]$-Sar$^1$-Ile$^8$-AngII as a tracer; each point represents the mean ± s.e.m. of two separate experiments, each performed in duplicates.

## Supplementary Material

Refer to Web version on PubMed Central for supplementary material.

## Acknowledgments

## References

1. Karnik SS, et al. International Union of Basic and Clinical Pharmacology. XCIX Angiotensin Receptors: Interpreters of Pathophysiological Angiotensinergic Stimuli. Pharmacol Rev. 2015; 67:754–819. [PubMed: 26315714]

2. de Gasparo M, Catt KJ, Inagami T, Wright JW, Unger T. International union of pharmacology. XXIII The angiotensin II receptors. Pharmacol Rev. 2000; 52:415–472. [PubMed: 10977869]

3. Zaman MA, Oparil S, Calhoun DA. Drugs targeting the renin-angiotensin-aldosterone system. Nat Rev Drug Discov. 2002; 1:621–636. [PubMed: 12402502]

4. Porrello ER, Delbridge LM, Thomas WG. The angiotensin II type 2 (AT2) receptor: an enigmatic seven transmembrane receptor. Front Biosci. 2009; 14:958–972.

5. Guimond MO, Gallo-Payet N. How does angiotensin AT(2) receptor activation help neuronal differentiation and improve neuronal pathological situations? Front Endocrinol. 2012; 3:164.

6. Berk BC. Angiotensin type 2 receptor (AT2R): a challenging twin. Sci STKE. 2003; 181:pe16.

7. Miura S, Matsuo Y, Kiya Y, Karnik SS, Saku K. Molecular mechanisms of the antagonistic action between AT1 and AT2 receptors. Biochem Biophys Res Commun. 2010; 391:85–90. [PubMed: 19896468]

8. Hein L, Barsh GS, Pratt RE, Dzau VJ, Kobilka BK. Behavioural and cardiovascular effects of disrupting the angiotensin II type-2 receptor in mice. Nature. 1995; 377:744–747. [PubMed: 7477266]

9. Ichiki T, et al. Effects on blood pressure and exploratory behaviour of mice lacking angiotensin II type-2 receptor. Nature. 1995; 377:748–750. [PubMed: 7477267]

10. Porrello ER, et al. Angiotensin II type 2 receptor antagonizes angiotensin II type 1 receptor-mediated cardiomyocyte autophagy. Hypertension. 2009; 53:1032–1040. [PubMed: 19433781]

11. Ruiz-Ortega M, et al. Angiotensin II activates nuclear transcription factor kappaB through AT(1) and AT(2) in vascular smooth muscle cells: molecular mechanisms. Circ Res. 2000; 86:1266–1272. [PubMed: 10864918]

12. Ruiz-Ortega M, Lorenzo O, Ruperez M, Blanco J, Egido J. Systemic infusion of angiotensin II into normal rats activates nuclear factor-kappaB and AP-1 in the kidney: role of AT(1) and AT(2) receptors. Am J Pathol. 2001; 158:1743–1756. [PubMed: 11337372]

13. Caballero R, et al. Interaction of angiotensin II with the angiotensin type 2 receptor inhibits the cardiac transient outward potassium current. Cardiovasc Res. 2004; 62:86–95. [PubMed: 15023555]

14. Zhao Y, et al. Angiotensin II induces peroxisome proliferator-activated receptor gamma in PC12W cells via angiotensin type 2 receptor activation. J Neurochem. 2005; 94:1395–1401. [PubMed: 15992368]

15. Guimond MO, Gallo-Payet N. The Angiotensin II Type 2 Receptor in Brain Functions: An Update. Int J Hypertens. 2012; 2012:351758. [PubMed: 23320146]

16. Anand U, et al. Angiotensin II type 2 receptor (AT2 R) localization and antagonist-mediated inhibition of capsaicin responses and neurite outgrowth in human and rat sensory neurons. Eur J Pain. 2013; 17:1012–1026. [PubMed: 23255326]

17. Smith MT, Woodruff TM, Wyse BD, Muralidharan A, Walther T. A small molecule angiotensin II type 2 receptor (AT(2)R) antagonist produces analgesia in a rat model of neuropathic pain by inhibition of p38 mitogen-activated protein kinase (MAPK) and p44/p42 MAPK activation in the dorsal root ganglia. Pain Med. 2013; 14:1557–1568. [PubMed: 23742186]

18. Smith MT, Wyse BD, Edwards SR. Small molecule angiotensin II type 2 receptor (AT(2)R) antagonists as novel analgesics for neuropathic pain: comparative pharmacokinetics, radioligand binding, and efficacy in rats. Pain Med. 2013; 14:692–705. [PubMed: 23489258]

19. Smith MT, Lau T, Wallace VC, Wyse BD, Rice AS. Analgesic efficacy of small-molecule angiotensin II type 2 receptor antagonists in a rat model of antiretroviral toxic polyneuropathy. Behav Pharmacol. 2014; 25:137–146. [PubMed: 24525712]

20. Rice AS, et al. EMA401, an orally administered highly selective angiotensin II type 2 receptor antagonist, as a novel treatment for postherpetic neuralgia: a randomised, double-blind, placebo-controlled phase 2 clinical trial. Lancet. 2014; 383:1637–1647. [PubMed: 24507377]

21. Wan Y, et al. Design, synthesis, and biological evaluation of the first selective nonpeptide AT2 receptor agonist. J Med Chem. 2004; 47:5995–6008. [PubMed: 15537354]

22. Kemp BA, et al. AT(2) receptor activation induces natriuresis and lowers blood pressure. Circ Res. 2014; 115:388–399. [PubMed: 24903104]

23. Larhed M, Hallberg M, Hallberg A. Nonpeptide AT2 Receptor Agonists. 2006; 51:69–82.

24. Zhang H, et al. Structure of the Angiotensin receptor revealed by serial femtosecond crystallography. Cell. 2015; 161:833–844. [PubMed: 25913193]

25. Zhang H, et al. Structural Basis for Ligand Recognition and Functional Selectivity at Angiotensin Receptor. J Biol Chem. 2015; 290:29127–29139. [PubMed: 26420482]

26. Glinka TW, et al. L-161,638: A potent AT2 selective quinazolinone angiotensin II binding inhibitor. Bioorg Med Chem Lett. 1994; 4:1479–1484.

27. de Laszlo, S., Glinka, T., Greenlee, W., Chakravarty, P., Patchett, A. Disubstituted 6-aminoquinazolinones. US Patent. 5,385,894. 1995.

28. Dosa PI, Amin EA. Tactical Approaches to Interconverting GPCR Agonists and Antagonists. J Med Chem. 2016; 59:810–840. [PubMed: 26390077]

29. Murugaiah AM, et al. From the first selective non-peptide AT(2) receptor agonist to structurally related antagonists. J Med Chem. 2012; 55:2265–2278. [PubMed: 22248302]

30. Chun E, et al. Fusion partner toolchest for the stabilization and crystallization of G protein-coupled receptors. Structure. 2012; 20:967–976. [PubMed: 22681902]

31. Caffrey M, Cherezov V. Crystallizing membrane proteins using lipidic mesophases. Nat Protoc. 2009; 4:706–731. [PubMed: 19390528]

32. Liu W, et al. Serial femtosecond crystallography of G protein-coupled receptors. Science. 2013; 342:1521–1524. [PubMed: 24357322]

33. Liu W, Ishchenko A, Cherezov V. Preparation of microcrystals in lipidic cubic phase for serial femtosecond crystallography. Nat Protoc. 2014; 9:2123–2134. [PubMed: 25122522]

34. Weierstall U, et al. Lipidic cubic phase injector facilitates membrane protein serial femtosecond crystallography. Nat Commun. 2014; 5:3309. [PubMed: 24525480]

35. Ballesteros, JA., Weinstein, H. Methods in Neurosciences. Stuart, C Sealfon, editor. Vol. 25. Academic Press; 1995. p. 366-428.

36. Katritch V, Cherezov V, Stevens RC. Structure-function of the G protein-coupled receptor superfamily. Annu Rev Pharmacol Toxicol. 2013; 53:531–556. [PubMed: 23140243]

37. Venkatakrishnan AJ, et al. Diverse activation pathways in class A GPCRs converge near the G-protein-coupling region. Nature. 2016; 536:484–487. [PubMed: 27525504]

38. Rasmussen SG, et al. Crystal structure of the beta2 adrenergic receptor-Gs protein complex. Nature. 2011; 477:549–555. [PubMed: 21772288]

39. Wacker D, et al. Structural features for functional selectivity at serotonin receptors. Science. 2013; 340:615–619. [PubMed: 23519215]

40. Katritch V, et al. Analysis of full and partial agonists binding to beta2-adrenergic receptor suggests a role of transmembrane helix V in agonist-specific conformational changes. J Mol Recognit. 2009; 22:307–318. [PubMed: 19353579]

41. Kang Y, et al. Crystal structure of rhodopsin bound to arrestin by femtosecond X-ray laser. Nature. 2015; 523:561–567. [PubMed: 26200343]

42. Katritch V, et al. Allosteric sodium in class A GPCR signaling. Trends Biochem Sci. 2014; 39:233–244. [PubMed: 24767681]

43. Balakumar P, Jagadeesh G. Structural determinants for binding, activation and functional selectivity of the AT1 receptor. J Mol Endocrinol. 2014; 53:R71–92. [PubMed: 25013233]

44. Unal H, Karnik SS. Constitutive activity in the angiotensin II type 1 receptor: discovery and applications. Adv Pharmacol. 2014; 70:155–174. [PubMed: 24931196]

45. Miura S, Karnik SS. Angiotensin II type 1 and type 2 receptors bind angiotensin II through different types of epitope recognition. J Hypertens. 1999; 17:397–404. [PubMed: 10100078]

46. Miura S, Karnik SS. Ligand-independent signals from angiotensin II type 2 receptor induce apoptosis. EMBO J. 2000; 19:4026–4035. [PubMed: 10921883]

47. Akazawa H, Yano M, Yabumoto C, Kudo-Sakamoto Y, Komuro I. Angiotensin II type 1 and type 2 receptor-induced cell signaling. Curr Pharm Des. 2013; 19:2988–2995. [PubMed: 23176210]

48. Hein L, Meinel L, Pratt RE, Dzau VJ, Kobilka BK. Intracellular trafficking of angiotensin II and its AT1 and AT2 receptors: evidence for selective sorting of receptor and ligand. Mol Endocrinol. 1997; 11:1266–1277. [PubMed: 9259318]

49. Widdop RE, Matrougui K, Levy BI, Henrion D. AT2 receptor-mediated relaxation is preserved after long-term AT1 receptor blockade. Hypertension. 2002; 40:516–520. [PubMed: 12364356]

50. Kabsch W. XDS. Acta crystallogr D Biol Crystallogr. 2010; 66:125–132. [PubMed: 20124692]

51. White TA, et al. Recent developments in CrystFEL. J Appl Crystallogr. 2016; 49:680–689. [PubMed: 27047311]

52. McCoy AJ, et al. Phaser crystallographic software. J Appl Crystallogr. 2007; 40:658–674. [PubMed: 19461840]

53. Emsley P, Lohkamp B, Scott WG, Cowtan K. Features and development of Coot. Acta crystallogr D Biol Crystallogr. 2010; 66:486–501. [PubMed: 20383002]

54. Bhat TN. Calculation of an Omit Map. J Appl Crystallogr. 1988; 21:279–281.

55. Chen VB, et al. MolProbity: all-atom structure validation for macromolecular crystallography. Acta Crystallogr D Biol Crystallogr. 2010; 66:12–21. [PubMed: 20057044]

56. Halgren TA. Potential energy functions. Curr Opin Struct Biol. 1995; 5:205–210. [PubMed: 7648322]

57. Totrov M, Abagyan R. Flexible protein-ligand docking by global energy optimization in internal coordinates. Proteins Suppl. 1997; 1:215–220.

58. Lee J, et al. CHARMM-GUI Input Generator for NAMD, GROMACS, AMBER, OpenMM, and CHARMM/OpenMM Simulations Using the CHARMM36 Additive Force Field. J Chem Theory Comput. 2016; 12:405–413. [PubMed: 26631602]

59. Humphrey W, Dalke A, Schulten K. VMD: visual molecular dynamics. J Mol Graph. 1996; 14:33–38. 27–38. [PubMed: 8744570]

60. Best RB, et al. Optimization of the additive CHARMM all-atom protein force field targeting improved sampling of the backbone $\varphi$, $\psi$ and side-chain $\chi(1)$ and $\chi(2)$ dihedral angles. J Chem Theory Comput. 2012:8.

61. Abraham MJ, et al. GROMACS: High performance molecular simulations through multi-level parallelism from laptops to supercomputers. SoftwareX. 2015; 1–2:19–25.

62. Berendsen HJC, Postma JPM, van Gunsteren WF, DiNola A, Haak JR. Molecular dynamics with coupling to an external bath. J Chem Phys. 1984; 81:3684–3690.

63. Hess B. P-LINCS: A Parallel Linear Constraint Solver for Molecular Simulation. J Chem Theory Comput. 2008; 4:116–122. [PubMed: 26619985]

64. de Laszlo SE, et al. The SAR of 6-(N-alkyl-N-acyl)-2-propyl-3-[(2′-tetrazol-5-yl)biphen-4-yl)methyl]-quinazolinones as balanced affinity antagonists of the human AT1 and AT2 receptors. Bioorg Med Chem Lett. 1995; 5:1359–1364.

65. de Laszlo SE, et al. The design, binding affinity prediction and synthesis of macrocyclic angiotensin II AT1 and AT2 receptor antagonists. Bioorg Med Chem Lett. 1996; 6:923–928.

66. Beauchamp HT, Chang RS, Siegl PK, Gibson RE. In vivo receptor occupancy of the angiotensin II receptor by nonpeptide antagonists: relationship to in vitro affinities and in vivo pharmacologic potency. J Pharmacol Exp Ther. 1995; 272:612–618. [PubMed: 7853174]
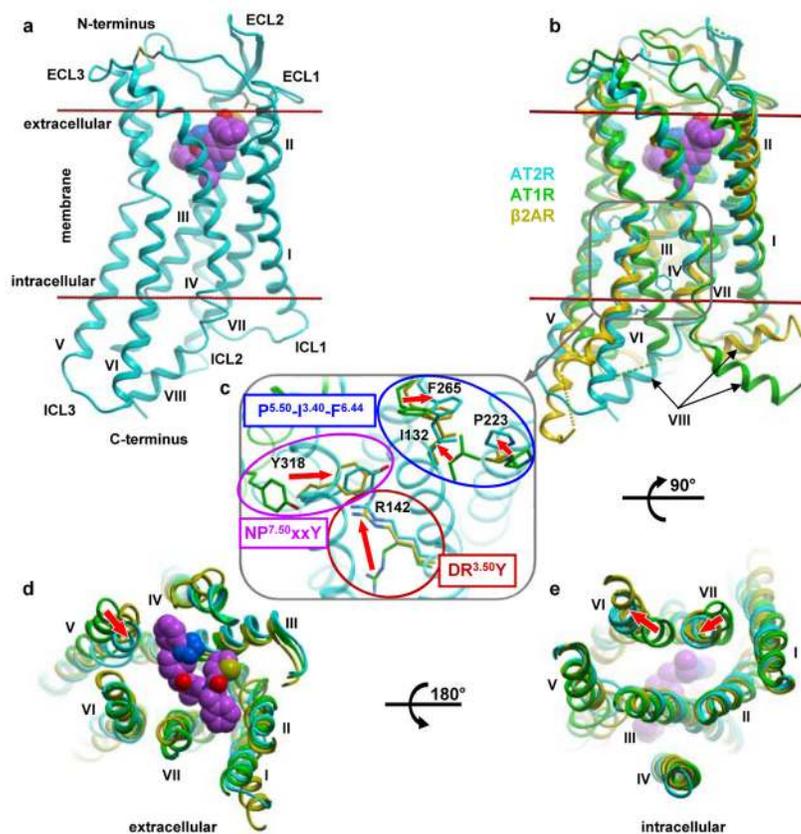
**Figure 1. Active-like conformation of AT$_2$R**

**a,** Overall receptor architecture. Cpd **1** is shown as spheres with carbon atoms in magenta, nitrogen in blue, oxygen in red, and sulfur in yellow. Membrane boundaries as defined by the OPM web server (www.opm.phar.umich.edu) are shown as red lines. **b–e,** Structural comparison of the active-like AT$_2$R (cyan) with the inactive AT$_1$R (green, PDB 4YAY), and active G protein-bound β$_2$AR (yellow, PDB 3SN6) viewed from within the membrane **(b)**, the extracellular side **(d)**, and the intracellular side with helix VIII removed **(e)**. The magnified region in **(c)** shows details of microswitches in the conserved motifs. The backbone of AT$_2$R is shown in cyan cartoon, while distinct inactive position of AT$_1$R helix VII is shown in green. Red arrows indicate conformational changes associated with receptor activation.
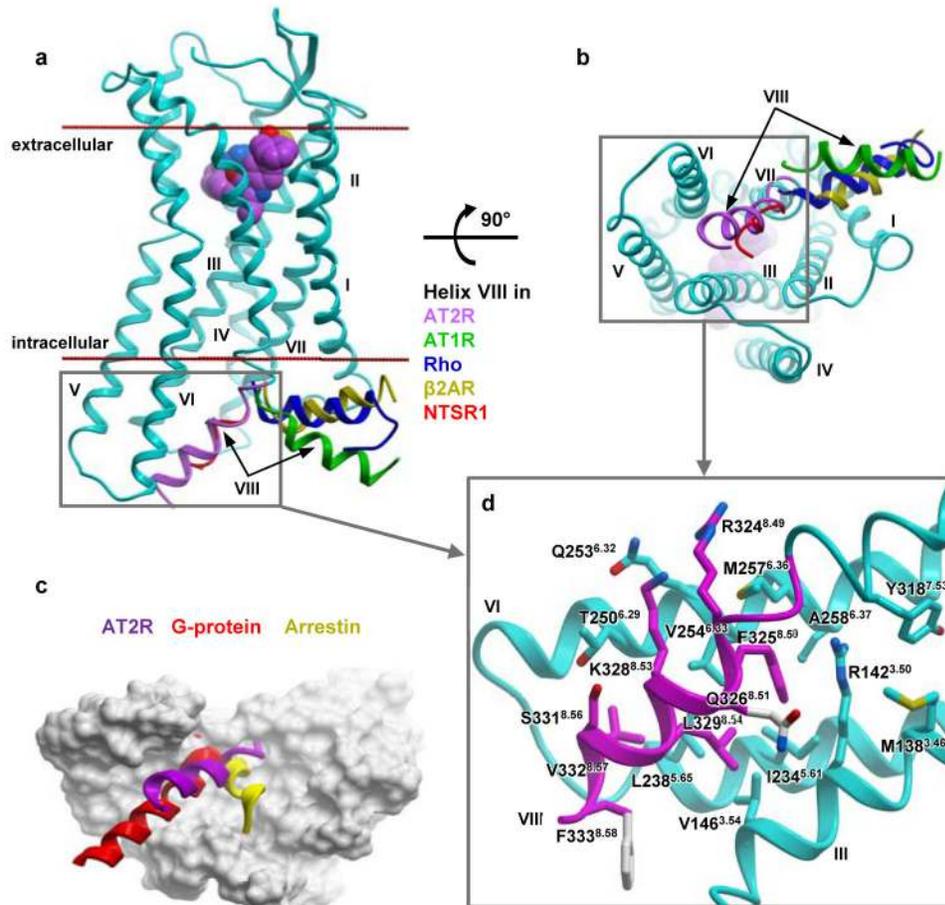
**Figure 2. Helix VIII blocks putative G protein/β-arrestin binding site of AT₂R**

**a, b,** Varied positions of helix VIII in different GPCRs shown as cartoons. AT$_2$R is in cyan with helix VIII colored magenta, AT$_1$R (PDB 4YAY) in green, NTSR1 (PDB 4GRV) in red, G protein-bound β$_2$AR (PDB 3SN6) in yellow, and arrestin-bound rhodopsin in blue (PDB 4ZWJ), viewed from within the membrane (**a**) and from the intracellular side (**b**). **c,** Shared interaction sites of AT$_2$R 7TM domain (grey surface) for the helix VIII of AT$_2$R (magenta), the C-terminus of G protein (red), and the finger loop of arrestin (yellow). **d,** interactions between helix VIII (magenta) and helices III, V, VI (cyan) in AT$_2$R. Side chains of helix VIII not resolved in the crystal structure are shown with grey carbon atoms.
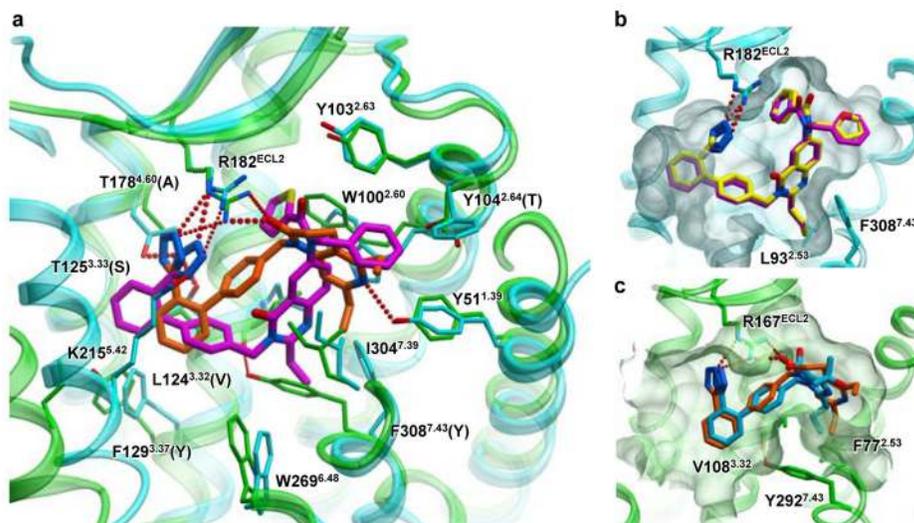
**Figure 3. Ligand selectivity between AT$_1$R and AT$_2$R**
**a,** Comparison of binding modes of different ligands in AT$_1$R (green) and AT$_2$R (cyan) binding pockets. The side chains in contact with ligands are shown as sticks with labels representing AT$_2$R and AT$_1$R residues in the corresponding positions. **b, c,** Comparison of the ligand-binding pockets between AT$_2$R (cyan) and AT$_1$R (green). Receptors are shown in the same orientation of transmembrane helices with the conserved Arg$^{ECL2}$ (Arg167$^{ECL2}$ in AT$_1$R and Arg182 $^{ECL2}$ in AT$_2$R) aligned. The ligands are shown as thick sticks, with carbon atoms of the AT$_2$R ligands Cpd **1** in magenta, Cpd **2** in yellow, the AT$_1$R ligands ZD7155 in orange, and olmesartan in blue.
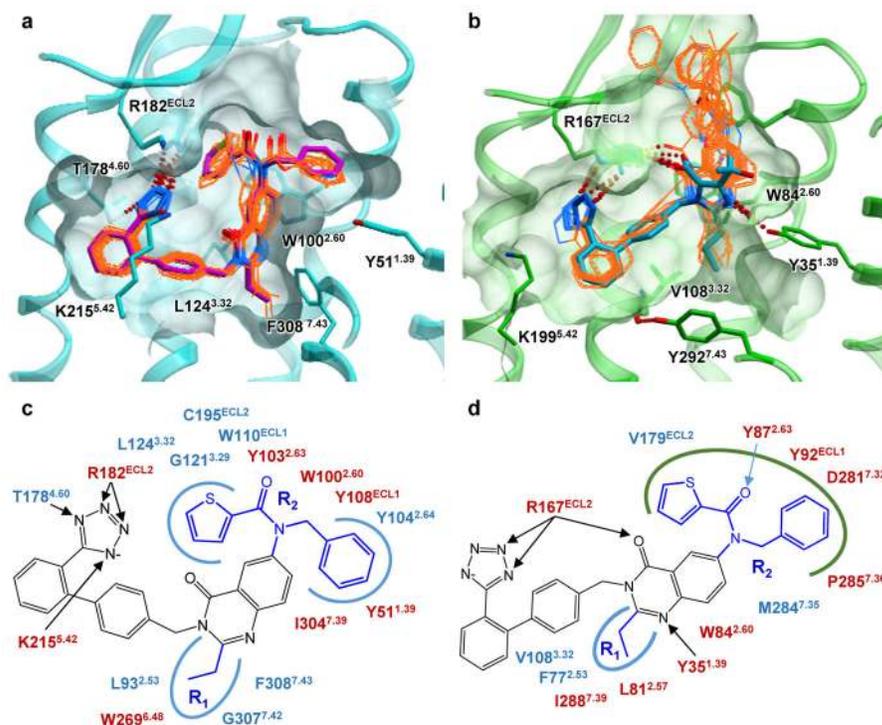
**Figure 4. Docking and SAR analysis of quinazolinone-biphenyltetrazole derivatives in AT$_2$R and AT$_1$R**

**a, b,** Docking poses for compounds from Extended Data Table 2 in the crystal structures of AT$_2$R (**a**) and AT$_1$R (**b**). Key side chains are shown as sticks. The ligands from the co-crystal structures, Cpd **1** for AT$_2$R and olmesartan for AT$_1$R, are shown as sticks with magenta and cyan carbons, respectively. The docked SAR analogs are shown as thin sticks with orange carbons. **c, d,** Schematics of interactions for docked compounds into AT$_2$R (**c**) and AT$_1$R (**d**) crystal structures. Residues conserved between AT$_2$R and AT$_1$R are shown in red, non-conserved residues are shown in blue. Well-defined hydrophobic pockets are shown as blue shapes, the loose hydrophobic pocket of AT$_1$R is shown as a green shape.